Patterns of anisotropic temperature factors in bovine trypsin crystals with and without 0.5 THz irradiation

Viktor Ahlberg Gagnér[1], Ida Lundholm[1], Maria-Jose Garcia-Bonete[1], Helena Rodilla[2], Ran Friedman[3], Vitali Zhaunerchyk[4], Gleb Bourenkov[5], Thomas Schneider[5], Jan Stake[2] and Gergely Katona[1,*]

[1] Department of Chemistry and Molecular Biology, University of Gothenburg, Gothenburg, Sweden.

[2] Department of Microtechnology and Nanoscience, Chalmers University of Technology, Gothenburg, Sweden.

[3] Department of Chemistry and Biomedical Sciences, Linnaeus University, Kalmar, Sweden

[4] Department of Physics, University of Gothenburg, Gothenburg, Sweden.

[5] European Molecular Biology Laboratory Hamburg Outstation, EMBL c/o DESY, Notkestrasse 85, 22603 Hamburg, Germany.

* Corresponding author, email: gergely.katona@cmb.gu.se

Abstract

Vibrational oscillations in amide and side chain groups are well studied in proteins, but these are not occupied at ambient temperatures and they have a short lifespan when infrared radiation is present. Active vibrational modes in proteins lie in the terahertz (THz) range at physiological temperatures, and their experimental descriptions of them in this range are lacking. In this paper, we present the effect of 0.5 THz irradiation on atomic displacement parameters (ADP) in bovine trypsin. The crystals were subjected to terahertz radiation in an alternating manner and two states of the crystals were recovered using X-ray crystallography. The clustering of ADPs uniquely identified atoms from the different crystals. The ADP similarities tended to develop between chemically similar atoms and between atoms of the catalytic triad. This pattern of ADP similarity is likely created by delocalized polar vibration modes rather than, as frequently assumed, elastic and rigid-body motions.

Studies of both macroscopic and nanoscale systems illustrate how damping forces can be counteracted by a low intensity but continuous energy supply. (*1*, *2*) The dynamics of protein molecules is also affected by friction (internal or due to the solvent), which is frequently assumed to lead to a positive damping of oscillations, In protein systems the typical question is what is the magnitude of damping effect (over, critical or underdamping), not the sign of the damping constant. (*3*) This is in line with experimental observations where momentary vibrational excitation of macromolecules undergoes rapid viscous damping at the picosecond scale (*4*, *5*) and the excitation energy dissipates to the environment in the form of thermal energy (thermalization). On the other hand, sustained self-oscillation of polar vibrations was predicted by Fröhlich (*6*) in biological dissipative systems (commonly referred to as Fröhlich condensation). The conditions that give rise to different degrees of this condensation have been investigated using simulations and appear to depend on the rates of excitation, the energy exchange between the phonon modes, thermalization and the temperature of the environment. (*7-10*)

The average density of terahertz optical phonons at room temperature (with mode energies <<kT) is already high even without external pumping at thermal equilibrium.(*11*) Intriguingly, sustained

self-oscillating phonons have been observed in WSe_2 2D nanostructures, which was then attributed to Bose-Einstein condensation of phonons at room temperature. The standing wave pattern disappeared at cryogenic temperatures. (*12*) Phonon-polaritons were also shown to undergo Bose-Einstein condensation in microcavities at thermal equilibrium. (*13*) In typical materials and molecular arrangements, however, the density of collective modes is not expected to be high enough for synchrony to occur spontaneously, (*14*) but this transition can be facilitated by external pumping. Collective phonons in biological systems are postulated to play a role in long-range protein-protein interactions, the adjustment of biochemical reaction rates and information processing in semicrystalline, supramolecular systems. (*7*, *15*) There is weak evidence that terahertz radiation affects biochemical reactions, (*16*) and microwave radiation affects living organisms.(*17*) In these cases, causality cannot be established without identifying a molecular mechanism behind the non-thermal effects claimed. Recently, structural changes associated with Fröhlich condensation were observed in lysozyme crystals when pumped with 0.4 THz radiation at room temperature, which suggests an experimental means to study such phenomena. (*18*) Continuous excitation of fluorophore-labelled bovine serum albumin with visible light has resulted in a sub-terahertz spectral signal, which evolved over minutes time scales. (*11*)

There are many examples of long-range allosteric effects in protein systems, in which dynamics play at least a partial role, as shown by NMR experiments. (*19-21*) Terahertz spectroscopy (*22*) was particularly successful in separating protein vibrations from the bulk solvent contribution and detected long-range vibrations in the protein scaffold. (*23, 24*) Terahertz spectroscopic measurements also revealed long-range dynamics linked to the functional state of proteins. (*25-27*) These experiments revealed that a mutation or binding of a small molecule at one site can affect the dynamics of one or more remote sites. Computational studies capture some aspects of correlated motions in proteins, (*28, 29*) but experimental benchmarks are often not strict enough for facilitating further improvements. As a general trend, long-range allostery is modeled as a cascading network of interactions from one point to another where the altered dynamics is stepwise transmitted through a chain of local interactions connecting distant sites. (*30, 31*) Local interactions still dominate in these network models and hence the influence they exert is expected to decay with increasing distance as it propagates in space.

In this study, the non-thermal effect of 0.5 THz radiation was investigated in bovine trypsin crystals cryo-cooled to 100 K. Optimization of the experimental geometry allowed us to collect wider diffraction angles. The resulting atomic resolution data revealed anisotropic displacements for individual atoms, which is key to understanding the dynamic relationship between them. The starting temperature is predicted to affect the non-equilibrium dynamics of biomolecules is predicted to be affected by although there is no consensus on the expected effect. (*7, 32*)

We analyzed the six ADPs of the atoms, which can be illustrated with “thermal” ellipsoids after diagonalization (Figure 1). The eigenvectors represent the axes of the ellipsoids and the eigenvalues represent the magnitudes of the displacements. For a typical protein atom, the magnitudes are not equal (the atom is anisotropic) and there is substantial crystal-to-crystals. To simplify the comparison of the ADPs, we adapted the B_{eq} (equivalent to an isotropic B-factors) (*33*) and anisotropy metrics (*34*) (henceforth ANISO). ANISO varies between zero and one, where one indicates perfect isotropy.

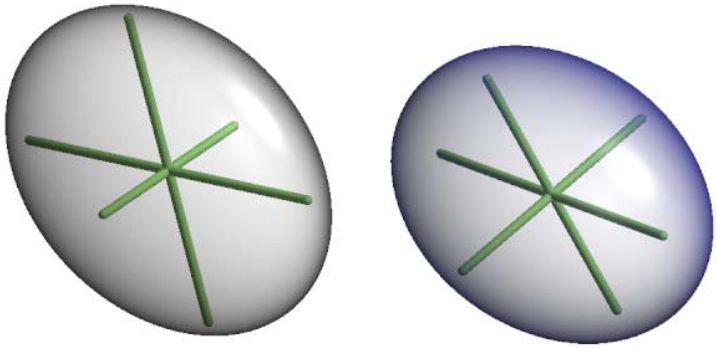

Figure 1 Thermal ellipsoids of the C (left) and N (right) atoms of Thr-125B located close to each other. The C and N display slightly oblate (pancake shape) and prolate (cigar shape) ellipsoids, respectively. The direction and length of the axes in the spheres are uniquely defined by eigenvectors and the corresponding eigenvalues of the ADP tensors. These two atoms are located in close vicinity to one other, but they display the highest similarity with distant atoms instead. The figure was obtained using RASTEP (*34*).

In addition to the traditional directionless metrics (B_{eq} and ANISO), we applied a metric-free hierarchical clustering approach to include directionality in the analysis. The inclusion of all the information from the ADPs dramatically improved the specificity of the clustering. Groups of atoms that share similar dynamics could be infered from the similarity of their positional probability distributions. The categorization of ADP changes is conceptually difficult for several reasons. Firstly, going from an U_{ij} matrix to a metric (such as B_{eq} and ANISO) inevitably involves a loss of information (converting six parameters to one). Secondly, it is unlikely that the changes affect only one metric (B_{eq} or ANISO). It is difficult to develop metrics that complement each other well. B_{eq} and ANISO form a reasonable combination, but they do not reveal anything about the directionality of thermal ellipsoids. Thirdly, even the initial diagonalization is problematic. For example, in (partially) isotropic atoms, the eigenvectors become arbitrary and their changes become meaningless and in practice are only influenced by errors. Fourthly, categorizing atoms based on which amino acid type they belong to can be considered artificial as well. Other distinctions may make more sense such as separating main chain from side chain atoms or grouping based on secondary structures, functional groups (carboxyl, hydroxyl, aromatic), etc.

In this article, the anisotropic displacements in the protein structure were analyzed at different length scales using different computational methods. We move stepwise from a global overview to atomic details. Initially, we discuss the effects of terahertz irradiation on individual amino residues by averaging the atomic data and comparing those results to simulated data. Finally, we elaborate on the effects on individual atoms related to terahertz dynamics using a clustering method.

Results

We irradiated orthorhombic bovine trypsin crystals alternately with a 0.5 THz radiation, such that the odd frames correspond to “THz on”-states and the even frames correspond to “THz off”-states. As a reference, we contrasted them with X-ray diffraction data collected from crystals that were not exposed to terahertz radiation. In contrast to an earlier experiment with hen egg white lysozyme,(*18*) bovine trypsin crystals were cryo-cooled to 100 K during the entire period of data collection with a dry nitrogen gas stream and suspended in a mylar loop without a surrounding

plastic capillary. In total, five terahertz irradiated and four reference crystals were retained for analysis. Data processing statistics are summarized in Table S1.

Comparison of the irradiated and non-irradiated state of the crystals reveal differences between individual residues

An initial comparison of the ADPs was based on the difference in B_{eq}-factor between equivalent atoms determined from the odd and even frames ($B_{eq,odd}-B_{eq,even}$). The mean and confidence interval (95%) of the difference in B_{eq}-factor for amino acid atoms were determined. Figure 2A shows this type of comparison for the twenty amino acids in the reference (*blue*) and terahertz irradiated crystals (*green*). B_{eq} appears to be either unchanged or similar to the references in the terahertz experiments except for the amino acid residue arginine. The B_{eq} of glycine, glutamine, serine, leucine and methionine atoms appear to decrease in odd data sets in the reference experiments.

The comparison of difference ANISO values (Figure 2B) shows a substantial overlap of confidence intervals (CI) between the reference and the terahertz categories. The CI derived from the reference and terahertz radiated crystal structures also included the value zero in most of the amino acid categories. The most notable exception was glycine residues, which showed an increased anisotropy (lower ANISO) upon terahertz irradiation. The position of the amino acid in the structure is important, therefore the ANISO value distribution of individual glycines, tryptophans and histidines are shown in Figure 3. From this comparison, it is obvious that most of the glycine residues behaved similarly in the terahertz radiation experiments compared to the references (Gly-43 is a clear exception), although in general, the atoms of the glycines in the N-terminal domain had a tendency to become more anisotropic when the crystals were subjected to terahertz radiation. Tryptophan residues became more anisotropic when all atoms were pooled together and Trp-51, Trp-215 and Trp-237 all had different average anisotropies in relation to the reference. Histidine residues, except His-57, appeared to be completely unaffected by terahertz radiation in the pooled comparison. As a general tendency, when there was a reversible change in anisotropy upon terahertz irradiation, it predominantly resulted in more anisotropic behavior in the residue atoms.

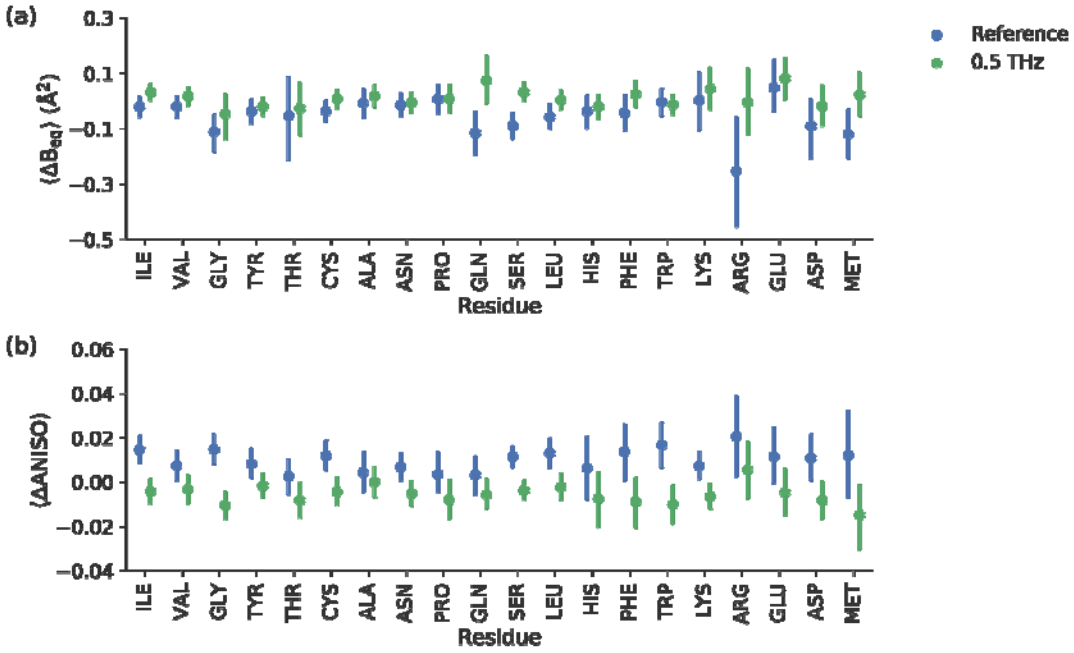

Figure 2 B_{eq}-factor and ANISO comparison between odd and even frames of the reference (*blue*) and terahertz irradiated (*green*) crystals in different types of amino acid residues. Each average is calculated from the difference in B_{eq} and ANISO for each individual atom in the reference and the terahertz irradiated crystals, respectively. The error bars represent 95 % confidence intervals for the mean.

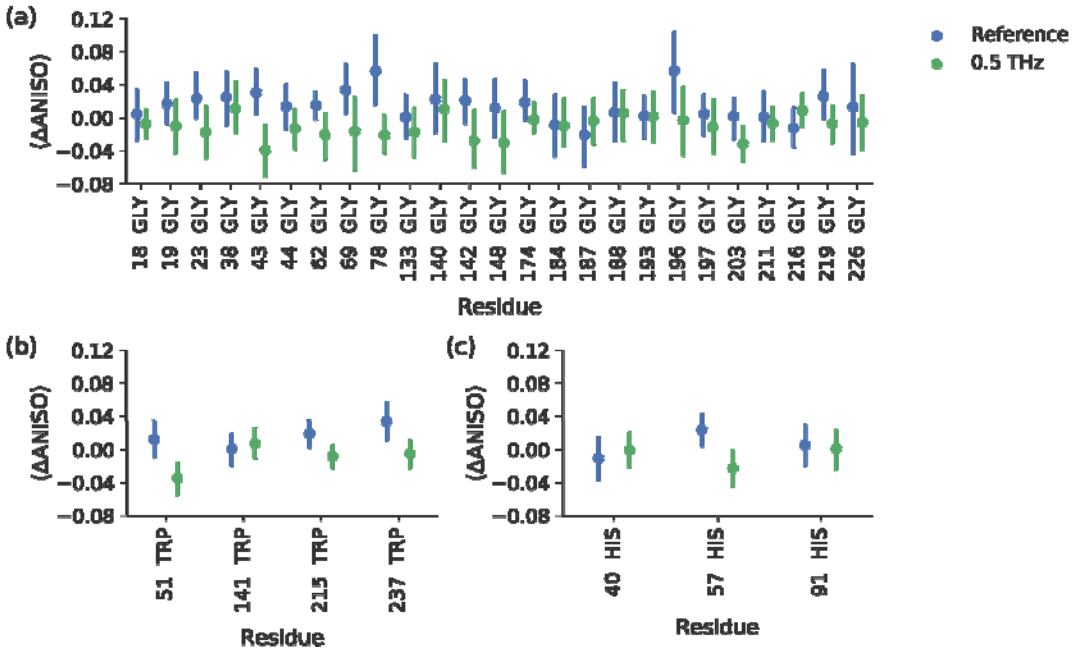

Figure 3 Comparison of ANISO change in selected amino acids (glycines, histidines and tryptophans) between odd and even frames of the reference (*blue*) and terahertz irradiated (*green*) crystals.

Comparison to NMA and MD simulations

In order to model ADP tensor components (U_{ij}) we performed NMA on an energy-minimized trypsin structure and generated random samples of the structure using all normal modes. The calculation assumed a temperature of 100 K. The B_{eq}s of predicted atomic U_{ij}s were approximately two orders of magnitude smaller than the experimentally observed values. Since NMA only explores the potential surface around a single minimum, it has a limited ability to follow protein dynamics, which consist of multiple conformations that exchange at slower than picoseconds timescales. Moreover, NMA is performed in a vacuum, which is not the case with solvated forms of proteins. Nevertheless, NMA is useful for inferring protein motions and hence we examined the correlation of NMA predicted U_{ij} metrics with Molecular Dynamics (MD) simulations and also with the experimental data.

An alternative to NMA is MD simulations of solvated protein molecules. In order to facilitate conformational changes, we performed the simulations at 300 K. When flash-cooling proteins, conformational variation is locked into a static distribution, but still affects the displacement parameters. Since conformational sampling is more delicate than sampling from an NMA ensemble, we used four MD simulations to predict the B_{eq} and anisotropy of the protein atoms and compared the values obtained to the corresponding parameters of the refined crystal structure (Figure 4). The predicted B_{eq} values were approximately on the same scale as the experimental values. They appeared to be underestimated for the well-ordered parts of the structure, but overestimated for the flexible regions. In particular, the B_{eq} of Tyr, Asn, Gln, Phe and Lys residues were greatly overestimated compared to the experimental data. There was a 0.53 Pearson correlation between the calculated (from segments of four times 10 ns simulations) and the experimental means of B_{eq} per residue (calculated for all equivalent atoms from the reference crystals). The mean ANISO values in amino acid residues show a smaller correlation (0.39), and MD simulations generally overestimate the anisotropy. By contrast, ANISO valuess derived from NMA simulations were more isotropic and agreed better with the experimental data. MD simulations predicted Asn residues to be much more anisotropic relative to other amino acid types as well (Figure 4D).

Perhaps it is unrealistic to expect good agreement of U_{ij} derived values between experiments and predictions on an absolute scale. For example, the simulation was performed at 300 K instead of 100 K. Despite this inconsistency, B_{eq} was found to be on approximately the same scale. This can be explained by the fact that conformational heterogeneity is frozen in the crystal when it is flash-cooled to 100 K. Anisotropy, on the other hand, may be incorrectly estimated at much higher temperatures. Nevertheless, one expects that B_{eq} will be estimated self-consistently and reproducibly by MD simulations. Since Pearson correlation coefficients (CC) are not affected by the absolute magnitudes of compared valuess, they are also a suitable measure for comparing crystal structure and predicted values (self- and cross-correlations). As Table S2 shows, the MD B_{eq} estimations are not stable and their correlation with the estimated B_{eq} decays over time. It does not matter which reference time point is chosen. For example, the simulated trajectory from MD1 had a B_{eq} CC of 0.83, 0.71 and 0.64 when compared to MD2, 3 and 4, respectively. Choosing MD2 as a starting point also shows a decreasing CC trend. NMA B_{eq} shows a substantially lower correlation with any of the MD predictions (the best correlation is 0.45). Moreover, when compared to the B_{eq} of crystal structures, earlier trajectories show higher correlations than later ones irrespective of the crystal structure to which they are compared (Table S3). NMA B_{eq} correlations with crystals is on par with some of the MD predictions (the best correlation is 0.45 to crystal x28 and x30). Reference crystal structures had B_{eq} CC in the range of 0.99-0.82 among themselves due to experimental and modelling variation (Table S4).

Anisotropy values showed a smaller correlation within the experimental data and also between the theoretical predictions, although the predictions seem to become more stable over time (Tables S5, S6) than the CCs for B_{eq}. Nevertheless, the combined experimental and modeling errors make predicted and experimental anisotropy hardly comparable (CC<0.4 for MD and CC<0.3 for NMA, Table S7). As such, we also have to consider the mismatch of the absolute level of anisotropy values between experiments and model predictions (Figure 4B). We provide additional discussion about the NMA and MD modelling in the Supporting Online Material.

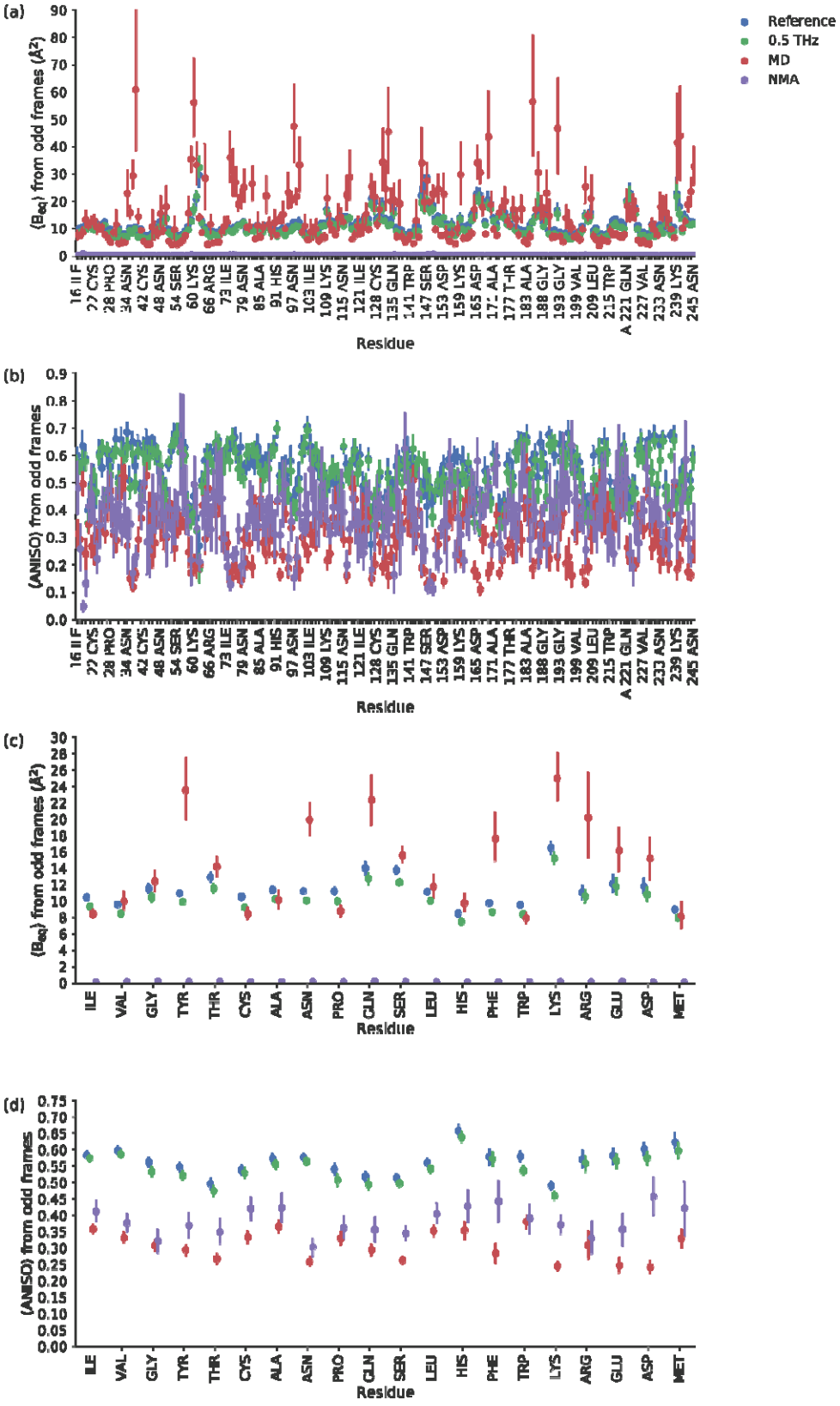

Figure 4 B_{eq}-factor and ANISO comparison based on the odd diffraction frames of reference crystals (*blue*) and odd diffraction frames of terahertz irradiated (*green*) crystals. MD (*orange*) and NMA (*purple*) mark the predictions from molecular dynamics simulations and normal mode analysis, respectively. Panels A and B show a comparison between the average properties of individual amino acid residues. Only every 4th residue is labelled to avoid overlaps of the labels. Panels C and D compare different amino acid types.

Metric-free clustering of atoms based on pairs of U_{ij} matrices

Hierarchical clustering was used in the crystallographic analysis, for example by grouping isomorphous crystals together (BLEND)(*35*) or detecting structural similarity.(*36*) In the context of analyzing ADPs, clustering algorithms have not been used before. Our atomic clustering was based on similarities between the components of ADP tensors, quantified by the Euclidean distance between the components (Figure 5). This way, atoms with similar shape, size and directionality are clustered together. The heat map represents the magnitude of the tensor components, providing quick visual feedback about the similarity and the nature of the remaining differences.

In Figure 5, the atoms from terahertz-radiated crystals are represented by green regions and these appear to cluster together. These atoms tend to originate from the core regions of the protein structure. The atom size, represented by the sum of the diagonal elements (B_{eq}), alone yields a very coarse clustering. However, slight differences in shape and orientation are enough to direct atoms to specific clusters.

Different, well-separated regions of the cluster correspond to different expectations as outlined above. In order to illustrate one type of formed clusters, Figure 6 zooms in on the top highlighted region in Figure 5. Here, we examine 7 out of 9 observations of the N_{ε} atom of Gln-135 on one branch. The immediately adjacent branch on the dendrogram consists of the N_{δ} atom of Asn-223, where all of the observations of this atom in all crystals can be found. It is worth emphasizing that no other information was used other than the 2 × 6 components of the U_{ij} matrices. Despite this, it is possible to uniquely identify up to 9 identical atoms from a total pool of 15921 atoms. These two atoms were not close to one other in the crystal structure, but they shared a similar position in a chemical group.

Figure 7 focuses on a central region highlighted in Figure 5, where most of the clustered atoms share the fact that they were observed in terahertz pumping experiments. The highlighted cluster contains three observations of C_{β} of Ser-195 and two observations of C_{β} of His-57. Ser-195 carries out the nucleophilic attacks and His-57 accepts the protons generated during the nucleophilic attacks. Atoms from Trp-215 and Ser-214 were also observed in this region. The backbone of these two amino acids form the antiparallel β-sheet with the substrate peptide in the Michaelis-complex and acyl-enzyme, and in addition the hydroxyl group of Ser-214 is hydrogen bonded to the third catalytic amino acid, Asp-102, which is not part of this cluster. The residue Trp-237 is represented with multiple atoms in the tree and this residue appears to be affected by terahertz radiation.

Figure 8 shows the lower marked region in Figure 5, where the link between His-57 and Asp-102 appears to be stronger. In particular, there is a similarity between $C_{\varepsilon 2}$ of His-57 and $O_{\delta 2}$ of Asp-102. In addition other $O_{\delta 2}$ atoms of functionally important aspartates seem to be tuned together: Asp-194, which forms a salt bridge with N-terminal Ile-16 converting the enzyme into its active form, (*37*) and Asp-189, which (in general) forms the salt bridge with the P1 residue of the substrate. In this crystal structure, the Asp-189 forms a salt bridge with the amidinium group of the inhibitor benzamidine. It is important to mention that atoms belonging to Trp-237 and Trp-51

also appear in these trees, as the anisotropy of these tryptophanes is affected by terahertz radiation.

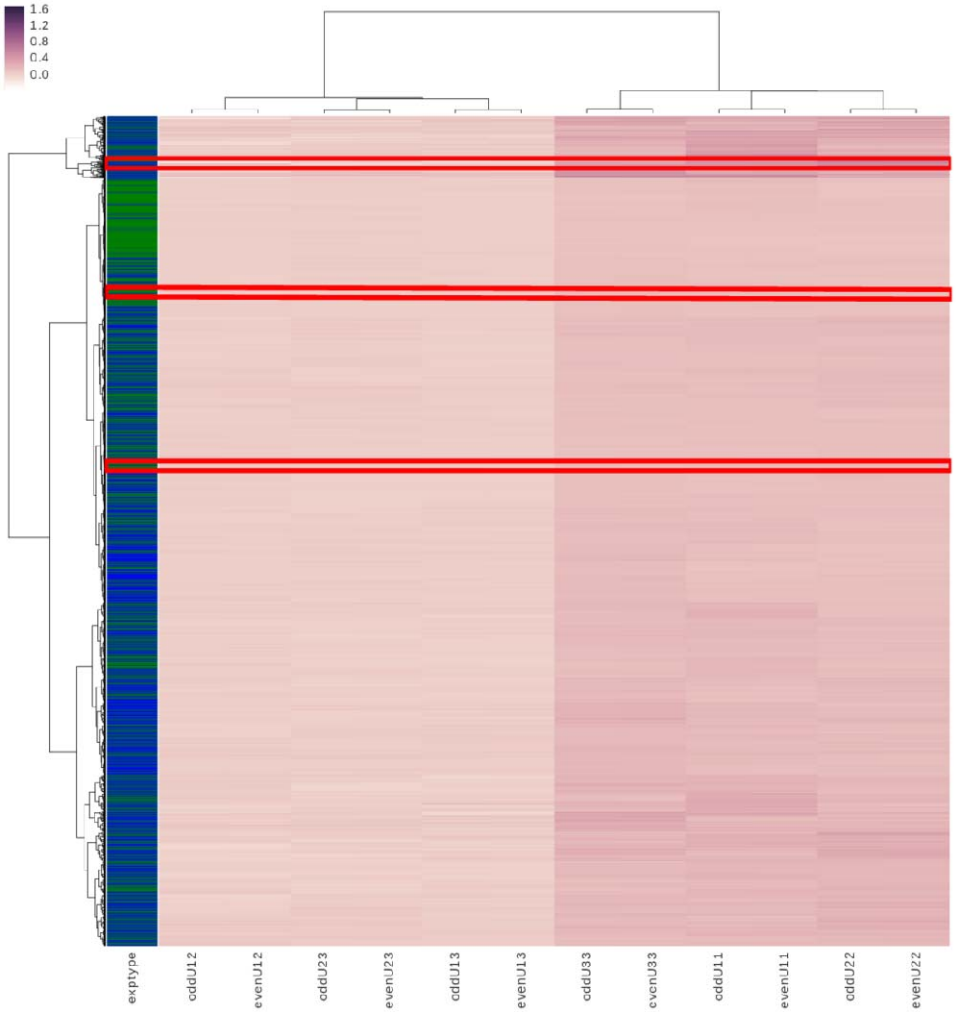

Figure 5 Cluster analysis of 15921 atoms of the two states (odd and even frames) of the four reference (*blue*) and five terahertz irradiated (*green*) crystals. Ideally, each line in the heat map and the corresponding green and blue color bar represent a single atom, but the resolution of this image is not sufficient to show all atoms. A more detailed view of the marked areas is shown in the subsequent plots. The dendrograms at the top and to the left represent the distances. The heat map represents the magnitude of each atom's ADP tensor components (U_{ij}) from the odd and the even state.

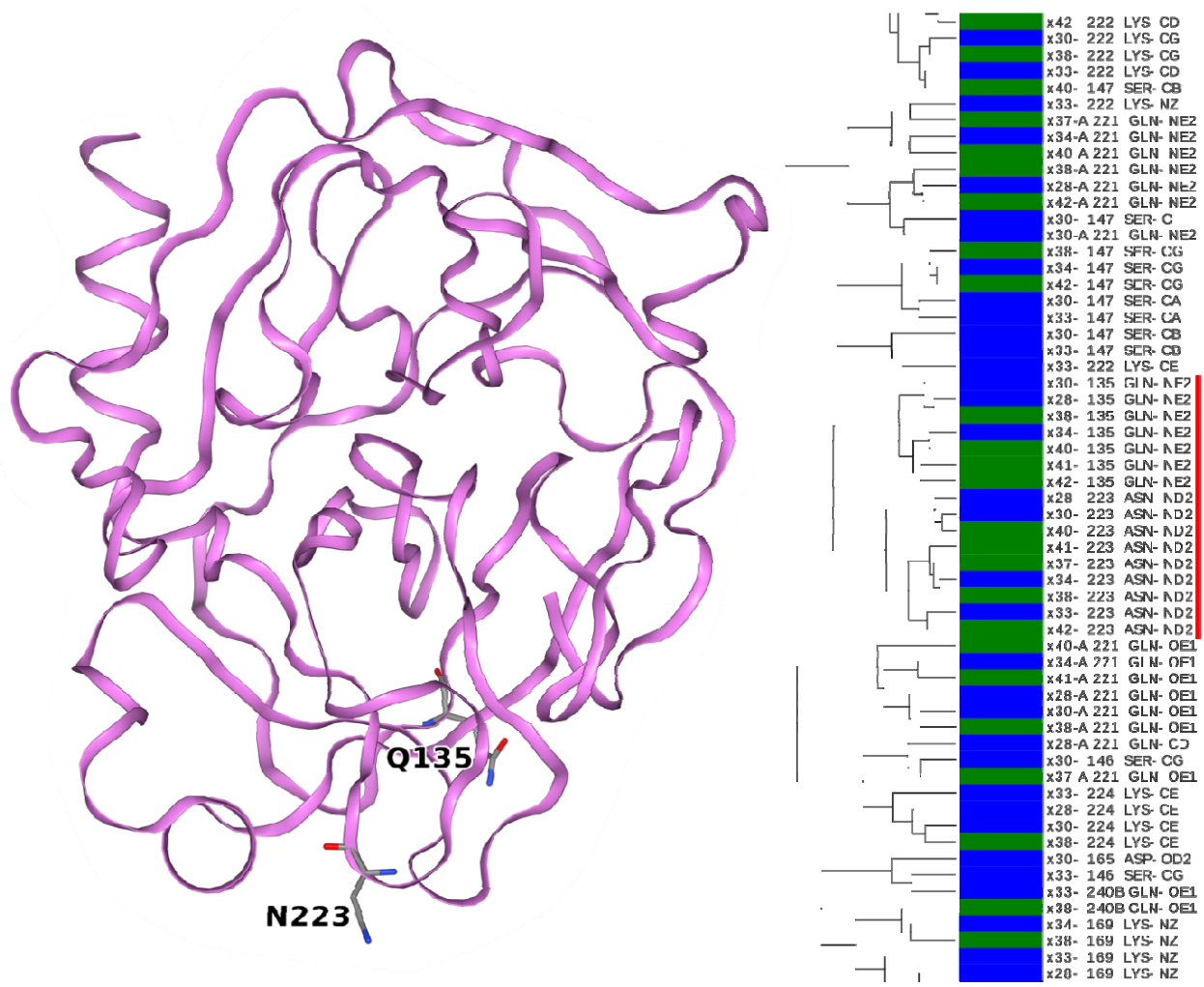

Figure 6 Clustering appears to identify amide nitrogen atoms of Gln-135 and Asn-223 residues in multiple crystals. (*red*) The two amino acids do not make intra- or intermolecular contacts. The trypsin structure is illustrated by a ribbon diagram. Those amino acid residues to which the clustered atoms belong are represented by sticks.

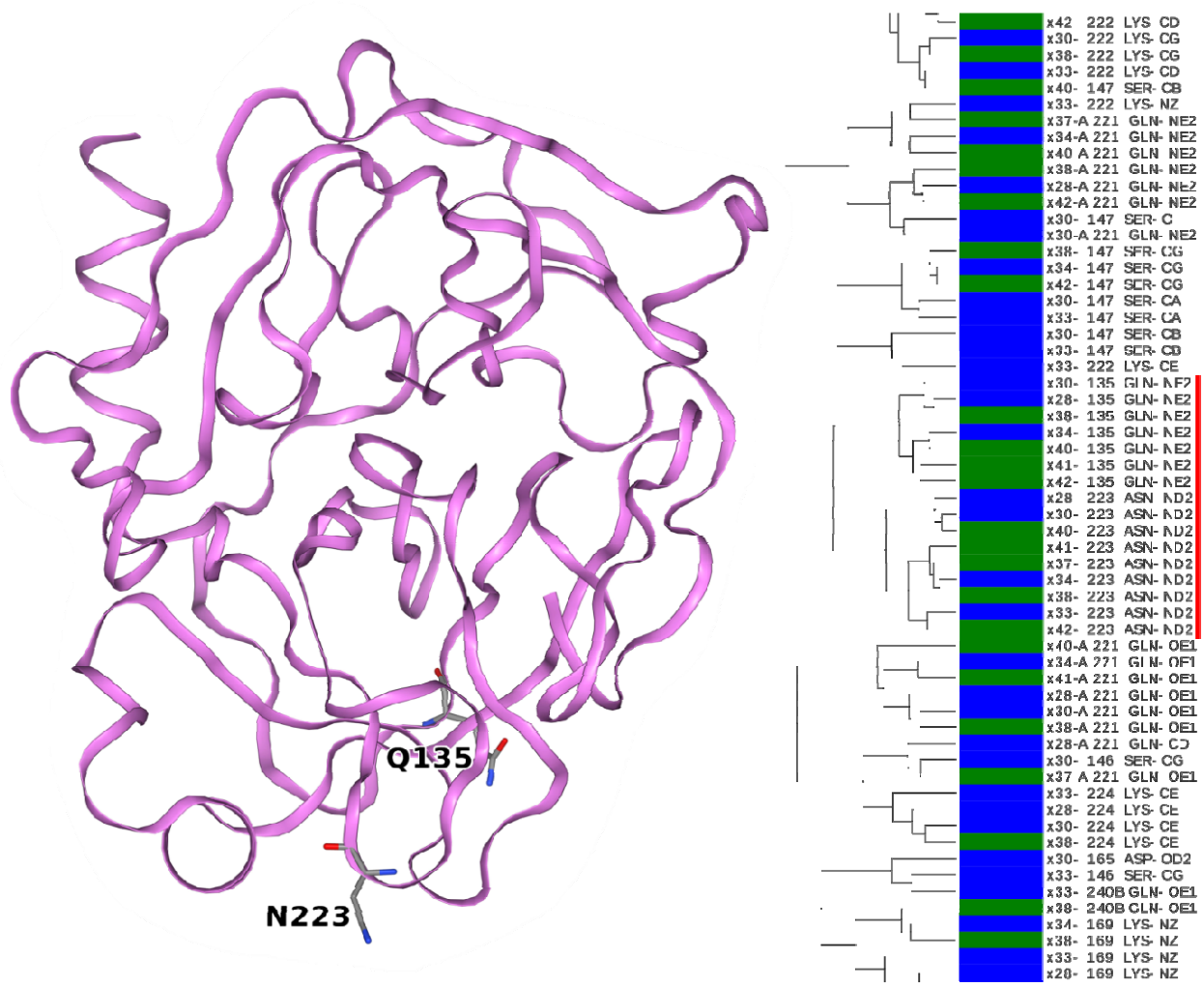

Figure 7 A cluster consisting of atoms from terahertz irradiated crystals that are involved in the catalytic process of the protein (Ser-195, His-57, Ser-214, Trp-215) and a high proportion of atoms originating from asparagine and tryptophan residues. The trypsin structure is illustrated by a ribbon diagram. Those amino acid residues to which the clustered atoms belong are represented by sticks.

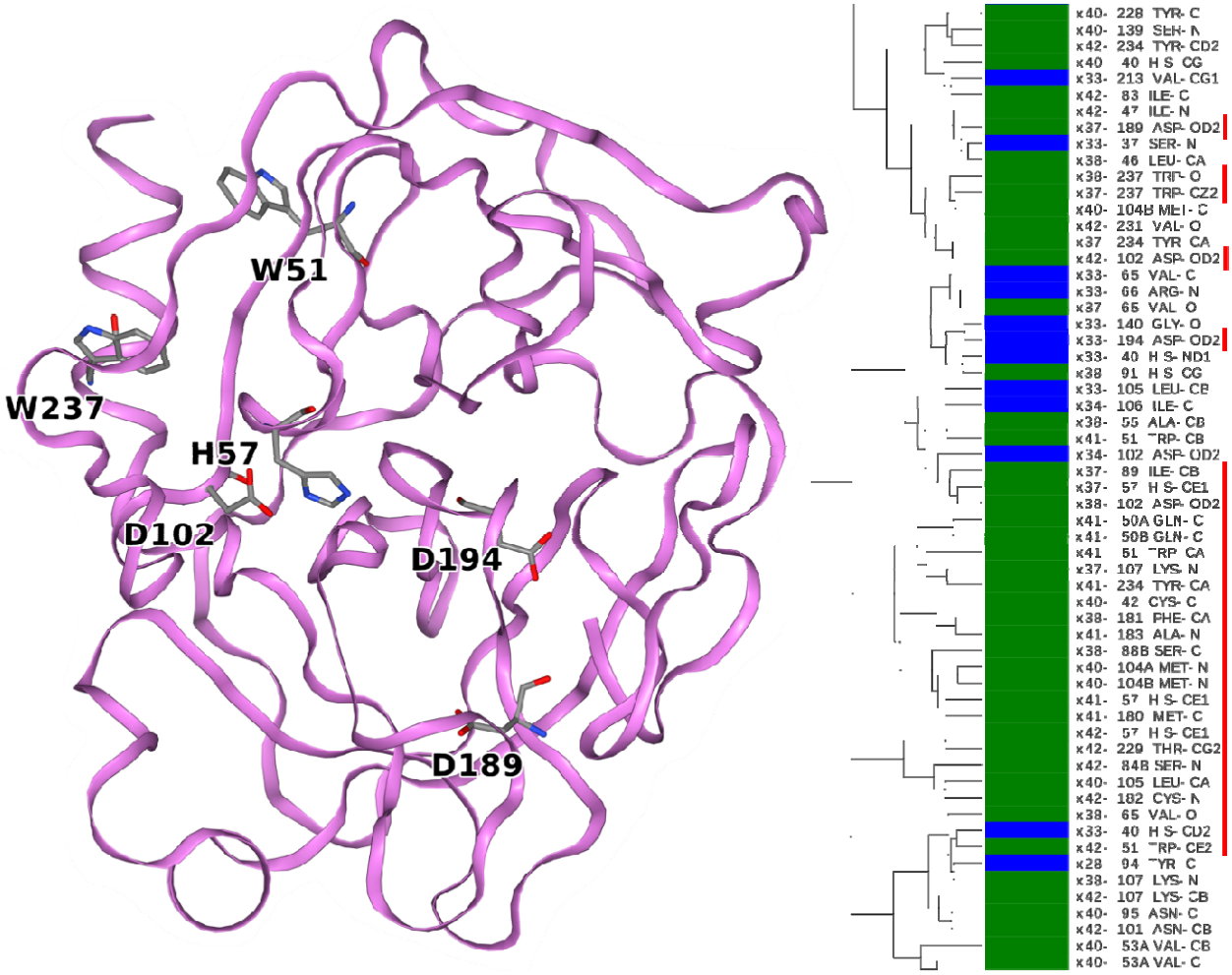

Figure 8 A cluster consisting of atoms from terahertz irradiated crystals that are involved in the catalysis and activation of trypsin (His-57, Asp-102, Asp-194 and Asp-189) a high proportion of atoms originating from tryptophan residues and all histidine residues are represented by atoms in the cluster. The trypsin structure is illustrated by a ribbon diagram. Those amino acid residues to which the clustered atoms belong are represented by sticks.

Discussion

The pattern of ADP clustering corresponds to trypsin function and reveals the dominance of polar vibrations

It is interesting to examine how the ADP clustering corresponds to the function of trypsin. Bovine trypsin is a serine protease that belongs to the chymotrypsin family. Its structure consists of two β-barrel domains that are stacked together and the catalytic triad of Ser-195, His-57 and Asp-102 amino acid residues are shared between them. (*38-40*) Trypsins cleave substrate peptides next to positively charged amino acid residues and the initial enzyme-substrate (Michaelis-) complex assumes an antiparallel β-sheet structure in which Ser-214, Trp-215 and Gly-216 participates from the enzyme's side. (*41*) The first step is that the Ser-195 hydroxyl group commits to a nucleophilic attack on the carbonyl carbon of the scissile peptide forming a short-lived covalent tetrahedral intermediate. This intermediate then breaks down to the first product and the acyl-enzyme intermediate where the second product is tightly held by an ester bond to Ser-195. The second nucleophilic attack comes from an activated water molecule, which

hydrolyzes the ester bond via a second tetrahedral intermediate. Both nucleophilic attacks are assisted by the His-57 - Asp-102 pair, which temporally accepts a proton from Ser-195, or from the activated water molecule, respectively. While the catalytic mechanism requires a subtle rearrangement of the active site atoms, there is a substantial energetic barrier to cross in order to overcome the remarkable stability of the peptide bond. The activation of the scissile peptide is partly provided by the polarizing effect of two main chain hydrogen bonds, termed the oxyanion hole, which is formed by the amide nitrogen atoms of Gly-193 and Ser-195. Longer substrates tend to be hydrolyzed faster which suggests that collective motions of the substrate-enzyme β-sheet contribute to the catalytic efficiency. (*41*) On the surface, it appears that the mechanism of trypsin catalysis is well understood, but we still lack a predictive model that associates a mutation or allosteric modulation with an expected change in catalytic parameters and substrate specificity. (*42*)

Atoms in functionally important residues appear repeatedly together in local clusters. Atoms in separate branches are often predominantly observed in either terahertz radiated or non-radiated crystals, respectively. In Figure 7, one such terahertz radiated branch (green) is highlighted. A large physical distance between these atoms does not appear to be a hindrance, whereas the chemical nature of the atoms clearly does have an influence. For example, not all carbon atoms are preferentially associated with other carbon atoms, but carbon atoms in α and β positions in the amino acid residues are different enough to sort them to different clusters. One could consider the ADP similarity to be an effect of the atom types having a similar partial charge. This could be a tempting assumption for the amide side chain nitrogen of asparagine and glutamine (Figure 6), which are assumed to have a strong and similar negative partial charge in most empirical force fields. It would also make sense that atoms with a similar partial charge respond similarly to a uniform electrostatic field. In a sodium chloride crystal, there are two well-defined charged ions (Na^+ and Cl^-), and these respond to electromagnetic (EM) fields in two possible ways. As a result, polar vibrations (optical phonons) emerge. In a protein, there is a whole palette of atom types, and we approximate each as having a specific static partial charge between approximately −0.8 and +0.9. Consequently, each of these atom types may have a slightly different response to EM fields. On the other hand, the origin of the terahertz EM field makes no difference. The EM field may be generated internally by the protein (crystal), by the solvent, by external pumping or any combination of these. Since the wavelength of terahertz EM waves is much longer than the size of protein molecules they generate virtually uniform EM fields across the protein molecule at any given moment. On the other hand, the partial charges of C_β atoms are not necessarily similar. For example, C_β of Ser-195 is assumed to be partially positive because of its bonding to the more electronegative hydroxyl group, whereas C_β of His-57 is assumed to be more neutral, because it is attached to another carbon of an imidazole ring. Nonetheless, these two C_β atoms reproducibly cluster together (Figure 7).

Do protein domain structures emerge from synchronization of local dynamics?

In architecture, you model the dynamics of an arbitrary structure (a house or a bridge) and then alter the structure until the dynamical properties are acceptable. Molecular NMA follows this same conventional logic, except that making planned changes in a protein structure is not a trivial process. In contrast to conventional engineering, a protein structure is not created by placing the atoms into arbitrary positions; rather, it emerges spontaneously from a quite dynamic polymer under suitable conditions (protein folding). Thus NMA is not practical for solving this hypothetical inverse problem (predicting a structure from polypeptide dynamics).

We show evidence here that in the folded, crystallized form of a protein, atomic fluctuations are characteristic, stationary (reproducibly seen in multiple crystal structures) and coordinated across long distances. At first glance, intriguingly, atoms of a sharply defined chemical nature align themselves with similar atoms in other identical chemical groups. Another non-random aspect is that atoms cluster together when they originate from terahertz pumped crystals (Figure 5 and 7). The dissipation of applied terahertz radiation enhances the clustering of atoms for example by grouping identical atoms from multiple crystals into the same cluster and placing atoms from functional residues to common groups. On the other hand, the ADPs in our reference crystals already provide substantial information about the long-range pattern: it is not exclusively present in condition out of equilibrium.

Our work shows that in a protein crystal structure some, but not all, similar atoms have similar ADPs. The mechanism for selecting from the many chemically similar atoms needs to be investigated further. It appears that protein atoms form an intercalating mosaic of coexisting lattices, where it is common to see atoms from the same amino acid residues ending up in different clusters. Perhaps the most noticeable, but certainly not exclusive, example is the group of tryptophan residues, where the indole ring is often approximated as a rigid aromatic plane with torsional fluctuations around two axes as the most important motions. In stark contrast to this simplistic picture, atoms within the indole ring cluster differently and share clusters with atoms in other tryptophan residues. Tryptophan residues are often difficult to replace by mutagenesis and play a key role in maintaining the thermodynamic stability of protein structures. They are one of the strongest promotor of ordered state. (*43*, *44*) They also appear to be reversibly affected by terahertz radiation.

The disorder-to-order transition is also facilitated by asparagine and threonine residues. (*44*) In particular asparagine residues were poorly described by MD simulations , which predict larger B_{eq} and lower ANISO in absolute terms and relative to other amino acid types (Figure 4C and 4B). It appears that in folded form, the side chain amides of asparagine residues undergo very limited fluctuations even in the absence of local interactions. Given the limited local contacts, MD simulations predict more positional freedom. In the terahertz experiments, some of the asparagine atoms also appear in clusters together with catalytic residues (Figure 7). This is probably more the exception than the rule, since asparagines and glutamines in general do not appear to be significantly affected by external pumping (Figure 2, Figure 4C and 4B). Asparagines do not readily maintain a periodic secondary structure in contrast to their chemical relative, glutamines. (*45*) Glutamine side chains have greater orientational freedom with multiple potential alignment possibilities and can presumably support multiple alternative stationary conformations leading to an increase in long-range disorder.

Evolutionary processes change the chemical composition of proteins and thus change protein structure very slowly. In contrast, post-translational and epigenetic modifications can introduce multiple chemical groups of identical nature (phosphorylation, sulfurylation, acetylation, methylation, etc.) rapidly. Presumably, these post-translational modifications interact in a similar manner and redefine the (stationary or non-stationary) positional distributions of atoms depending on the pattern of the modifications. A particular example is the nucleosome histone subunits (H3, H4), each possessing highly dynamic N-terminal regions that are subject to epigenetic regulation through a combination of phosphorylation, methylation and acetylation at specific amino acid residues. Each combination of modifications has a finely tuned functional consequence, which several nucleosomes carry out in a concerted manner with considerable

distance between them. These modifications include promotion and silencing of gene transcription, unpacking of DNA and the formation of heterochromatin.

Delocalized polar vibrations are important for structure and function prediction

Physical proximity and local complementarity have been and still are the primary guiding principles in protein engineering. Directed engineering of protein interfaces is less than straightforward due to the elusive (allosteric) influence of the rest of the structure. The similarity of parameters that describe fluctuations are not routinely analyzed, however. B_{iso}-factors and NMR relaxation parameters by themselves do not contain much information: two atoms can easily have similar parameters, just by coincidence. Experimental and modeling errors make the comparison even more difficult. It requires series of observations (*46*, *47*) in order to recognize the covariance of these parameters and assign multiple atoms to a specific functional role. With anisotropic ADPs, the chances of coincidental similarities are dramatically reduced. While multiple related structures help (as demonstrated in this study), it is possible to detect similarities between atoms with good confidence even in a single crystal structure. The examples described here show that the anisotropy of these fluctuations appears to have a functional relevance with two or more atoms with similar ADPs being responsible for a similar function (catalysis, activation). These similarities can be revealed faster than time-consuming mutagenesis studies, which are also impossible when main chain atoms are concerned. While the extracellular enzyme trypsin is not typically seen as an allosteric enzyme, its substrate specificity, activation, and inhibitor binding involve diffusely distributed, concerted action of distant amino acid atom positions suggesting that the basis of allostery is a universal, emergent and dynamic process.

The identification of similar ADPs in a macromolecular structure is just the first essential step and there may be other regular relationships between ADPs (linked to some other aspects of atoms) than similarity. The second and possibly more difficult step is to find and understand the geometric patterns between atoms belonging to the same ADP cluster. Since similar ADPs seem to be linked to the chemical nature of atoms, empirical geometric rules may be recognized or applied in the absence of ADP observations. These patterns would then assist the development of long-range ADP restraints, replacing restraints based on bonding connectivity and positional proximity for which we found little experimental support. Improved ADP restraints may provide better electron density maps and more detailed structural models at lower crystallographic resolutions. More importantly, long-range geometric patterns between chemically similar atoms coupled to effective random conformational sampling may be able to assist the *de novo* prediction of protein structures.

Conclusions

Our study focused on two inseparable questions: the effect of terahertz radiation on protein crystals and the terahertz dynamics of folded proteins. We used crystallographic ADPs to measure the effect of terahertz radiation on crystals cooled to 100 K. Locally, we observed an increase in anisotropy and we focused our attention on glycine and tryptophan residues, and the catalytic residue His-57, where the most obvious changes in anisotropy occur. The clustering of atoms based on their ADPs provided a relational map, which complements the positional analysis of atoms based on their proximity. The clustering revealed that chemically similar atoms tend to have more similar ADPs even with a longer distance between them. We performed NMA and MD simulations to predict ADPs and achieved limited success only. It appears that that rigid body approximation, even at the level of small structural moieties such as amino acid side chains,

does not provide natural clusters for ADP similarities. An alternative model of liquid-like dynamics is not suitable either, because it does not predict long-range similarities. It appears that crystalline solids, small molecules, different thermodynamic states of macromolecules (*48*) and liquids have sufficiently distinct dynamics that ADP predictions of their dynamical models are not likely to be directly transferable. Biomolecular disorder incorporates diffusive motions of folded and unfolded domains relative to one other, conformational changes, elastic stretching, bending and torsions. On the other hand, our study demonstrates that within a folded unit polar terahertz vibrations dominate.

Methods

Protein crystallization and flash cooling

Bovine trypsin (Sigma) was dissolved in 30 mM HEPES pH 7.0, 3 mM $CaCl_2$ and 6 mg/ml benzamidine to obtain 60 mg/ml protein solution. Trypsin was crystallized using the hanging drop vapor diffusion method, by mixing 5 µl protein solution and 5 µl of precipitant solution (18% PEG8000, 50 mM HEPES pH 7.0, 0.2 M Ammonium sulfate, 3 mM $CaCl_2$ and 6 mg/ml benzamidine). After 3 days, orthorhombic crystals appeared with approximate dimensions of 100-300 µm. The crystals were harvested and soaked in cryoprotectant solution (additional 33% glycerol) for 1-2 seconds prior to flash cooling in liquid nitrogen.

X-ray diffraction data collection

X-ray diffraction data were collected at the EMBL P14 beamline in Hamburg. The incident X-ray beam was focused to a 10 µm horizontal × 50 µm vertical rectangular area at the sample position. The photon energy of the beam was 14 keV and the beam was attenuated to a photon flux of 4×10^{11} photons/s. The central panels of the Pilatus 6M-F detector were used (2463 × 2527 pixels) and the detector was placed at the distance of 130.4 mm from the crystal. We discuss the effect of X-ray radiation damage on ADPs in the Supporting Online Material and Figure S1.

The crystals were oriented with the minikappa goniometer such that the normal vector of clean crystal surface was aligned with the spindle direction. The beam cross section was positioned less than 100 µm from the crystal surface and 20 µm offset from the spindle axis. During X-ray exposure the crystals were continuously rotated with 0.4 °/s while the Pilatus 6M-F was continuously recording images at 25 ms intervals. During each image recording period, the detector spent 22 ms with photon counting and 3 ms with I/O operations (read out).

The terahertz radiation was generated by an amplifier / frequency multiplier chain (X32 stage AMC, manufactured by Viginia Diodes Inc., Charlottesville, VA), which was driven by a MG3692c microwave signal generator (Anritsu). The input microwave radiation was set to 15.625 GHz (10 mW), which resulted in 0.5 THz radiation (1 mW). The diagonal horn antenna (WR-2.2) was positioned approximately at 0.5 cm from the crystals. Under the assumption of a Gaussian beam profile, the THz spot size was approximately 4 mm. This estimate assumes a waist radius of 1.3 mm and that the beam originates from approximately 1/3 inside the antenna. We examine the thermal effect of the terahertz radiation in the Supporting Online Material.

To reduce systematic differences associated with thermal effects, the terahertz radiation source was operated alternately. A DG645 pulse (delay) generator (Stanford Research Systems) was triggered on the raising edge of the EN OUT signal of the Pilatus 6M-F detector. Upon triggering, the pulse generator was programmed to send a 23.5 ms pulse to the terahertz radiation source (THz_{on} period). Simultaneously, the pulse generator was set to ignore subsequent triggers

for 40 ms. Consequently, every odd numbered image was taken from the crystal in the terahertz irradiated state whereas the even numbered images recorded the diffraction image of the crystal in the non-irradiated state.

Odd and even numbered diffraction images still contained sufficiently super sampled measurements to integrate their total intensity independently. (*18, 49*) This applies even for the widest-angle reflections recorded for this study, observed far away from the spindle axis.

X-ray diffraction data analysis

The first diffraction image was always affected by the slow opening of the millisecond shutter and this image had systematically lower recorded scattering intensity. The data processing program XDS (*50*) uses the first image of each data set for initial scale, which introduced a systematic difference between the data sets based on odd and even images. Therefore, the first odd and first even images of each data set were removed from subsequent analysis. In addition, the kappa goniometer shadow was identified in each data set and the affected images were removed. Even number of images were removed in order to maintain the equal number of odd and even numbered diffraction images.

The sets of diffraction images, from the odd and even frames of each crystal were processed separately. By comparing the data and refinement statistics, we selected the crystals with generally high data quality, shown in Table S1. This pre-selection yielded 18 data sets, recorded from four reference and five terahertz radiated crystals. Moreover, since the frames affected by the goniometer shadow differed from crystal to crystal, the unaffected rotation wedges were integrated individually. The indexing and integration steps were carried out with the default settings in XDS. The subsequent scaling and merging were performed using the programs XSCALE and XDSCONV of the XDS package, respectively. In both programs, the standard settings for non-anomalous diffraction data were used.

Similarly, the subsequent model building and structural refinement were performed on each individual state (the odd and the even frames) of the individual crystals, using Refmac5 of the CCP4 package. (*51*) A previously refined model was used as a basis for the Refmac5 refinement (see Supporting Online Information).

Model building and structural refinement

A single starting model was refined against the 18 data sets (9 crystals, recorded on odd and even diffraction images). Refinement statistics is shown in Table S1.

The initial structure was based on pdb entry 4I8G, and the structure was solved by molecular replacement. (*52*) The starting model included 2058 non-hydrogen atoms 111 of which belonged to water molecules, 15 were heteroatoms and 1932 were part of amino acid residues. Riding hydrogen atoms were included during refinement. The initial refinement leading to a starting model is described in the Supporting Online Information.

The individual crystal refinement was carried out with Refmac5, using the rigid body, restrained isotropic and restrained anisotropic refinement procedures. Each refinement procedure was performed with the default settings for 100 cycles with an automatic weighting of restraints.

ADP analysis and clustering

The calculations and visualization were performed with the help of the python libraries numpy, scipy, pandas,(*53*) cctbx,(*54*) seaborn and NGLView. (*55*) Through hierarchical clustering, all the

observed atoms were iteratively grouped using the distance between their unmodified U_{ij} matrices. By having two observations of each atom in the same crystal, we obtained two symmetric U_{ij} matrices with six unique elements each. The clustering was thus performed in a twelve-dimensional data space and we used the Euclidian distance between these points. For clustering, Ward's method was used. (*56*)

Apparent X-ray dose calculations

In order to compare the apparent absorbed doses in the different crystal structures first we estimated the cumulative absorbed X-ray dose corresponding to each diffraction image. The absorbed dose was calculated using the program RADDOSE 3D. (*57*) The apparent dose was calculated as the product of the dose per frame, multiplied with the weighted arithmetic mean of the number of frames for each crystal.

Normal mode analysis and molecular dynamics simulations

Normal mode analysis (NMA) was performed using the Gromacs simulation package (*58-60*) version 2018-2, compiled with double precision. The structure was first energy minimized rigorously by employing several cycles of Steepest Descents and Conjugate Gradients energy minimization cycles. The CHARMM36 (*61-63*) force field was used in all calculations. Electrostatics and van der Waals forces were truncated at 1.8 nm with a shift cutoff from 1.5 nm. After energy minimization, the Hessian matrix was diagonalized and all eigenvalues and eigenvectors were used except the first six rotational and translational modes. An ensemble of structures was generated at 100 K by the Gromacs program gmx nmens and ADPs were calculated by the Gromacs program gmx rmsf for all non-hydrogen protein atoms.

Molecular dynamics simulations were carried out using energies and forces as implemented in the OPLS-AA/L force field. (*64*) The protein was solvated in a cubic box so that the minimum distance between any protein atom and the edge of the box was 1.0 nm. The water molecules were modeled with the TIP3P approach. (*65*) Cl^- ions were added in order to neutralize the charge. Before the MD simulation, internal constraints were relaxed by energy minimization. After the minimization, a restrained MD run was performed for 20 ps. During the restrained simulations, protein heavy atoms were fixed to their initial positions with a force constant of 1000 kJ mol^{-1} nm^{-2}. The restraints were released and the system was equilibrated for 60 ns before data collection for analysis.

The temperature was kept constant (T=300K) by use of the velocity-rescaling algorithm (τ_T=0.1 ps). (*66*) The pressure was coupled to an external bath with Berendsen's coupling algorithm(*67*) (P_{ref}=1 bar, τ_P=1 ps) during the equilibration and with the Parrinello–Rahman algorithm(*68*) afterwards. Van der Waals forces were truncated at 1.0 nm with a plain cutoff. Long-range electrostatic forces were treated using the particle mesh Ewald method.(*69*) Dispersion correction was applied for the energy and pressure.

After equilibration, the remaining 40 ns of simulations were divided into 10 ns segments and the ADPs were calculated with the Gromacs program gmx rmsf from the trajectory segments.

Acknowledgements

This work was supported by the Swedish Research Council, the Röntgen-Ångström Framework and the Knut and Alice Wallenberg Foundation. The diffraction experiments were performed at the P14 beamline of Petra III.

References

1. K. Y. Billah, R. H. Scanlan, Resonance, Tacoma Narrows bridge failure, and undergraduate physics textbooks. *American Journal of Physics* **59**, 118-124 (1991).
2. T. Barois, S. Perisanu, P. Vincent, S. T. Purcell, A. Ayari, Frequency modulated self-oscillation and phase inertia in a synchronized nanowire mechanical resonator. *New J Phys* **16**, (2014).
3. L. Meinhold, J. C. Smith, A. Kitao, A. H. Zewail, Picosecond fluctuating protein energy landscape mapped by pressure-temperature molecular dynamics simulation. *Proc. Natl. Acad. Sci. USA* **104**, 17261-17265 (2007).
4. D. Arnlund *et al.*, Visualizing a protein quake with time-resolved X-ray scattering at a free-electron laser. *Nat Methods* **11**, 923-926 (2014).
5. T. R. Barends *et al.*, Direct observation of ultrafast collective motions in CO myoglobin upon ligand dissociation. *Science* **350**, 445-450 (2015).
6. H. Fröhlich, Long-range coherence and energy storage in biological systems. *International Journal of Quantum Chemistry* **2**, 641-649 (1968).
7. J. R. Reimers, L. K. McKemmish, R. H. McKenzie, A. E. Mark, N. S. Hush, Weak, strong, and coherent regimes of Frohlich condensation and their applications to terahertz medicine and quantum consciousness. *Proc. Natl. Acad. Sci. U. S. A.* **106**, 4219-4224 (2009).
8. J. Preto, Semi-classical statistical description of Frohlich condensation. *Journal of biological physics* **43**, 167-184 (2017).
9. V. Salari, J. Tuszynski, M. Rahnama, G. Bernroider, Plausibility of quantum coherent states in biological systems. *J Phys Conf Ser* **306**, (2011).
10. M. V. Mesquita, A. R. Vasconcellos, R. Luzzi, Near-dissipationless coherent excitations in biosystems. *International Journal of Quantum Chemistry* **60**, 689-697 (1996).
11. I. Nardecchia *et al.*, Out-of-Equilibrium Collective Oscillation as Phonon Condensation in a Model Protein. *Phys Rev X* **8**, 031061 (2018).
12. I. Altfeder *et al.*, Scanning Tunneling Microscopy Observation of Phonon Condensate. *Sci Rep* **7**, 43214 (2017).
13. Y. Sun *et al.*, Bose-Einstein Condensation of Long-Lifetime Polaritons in Thermal Equilibrium. *Phys Rev Lett* **118**, 016602 (2017).
14. T. Byrnes, N. Y. Kim, Y. Yamamoto, Exciton-polariton condensates. *Nat Phys* **10**, 803-813 (2014).
15. J. Preto, M. Pettini, J. A. Tuszynski, Possible role of electrodynamic interactions in long-distance biomolecular recognition. *Phys Rev E* **91**, 052710 (2015).
16. A. Homenko, B. Kapilevich, R. Kornstein, M. A. Firer, Effects of 100 GHz radiation on alkaline phosphatase activity and antigen-antibody interaction. *Bioelectromagnetics* **30**, 167-175 (2009).
17. M. Wyde *et al.*, Report of Partial findings from the National Toxicology Program Carcinogenesis Studies of Cell Phone Radiofrequency Radiation in Hsd: Sprague Dawley® SD rats (Whole Body Exposure). (2018).
18. I. V. Lundholm *et al.*, Terahertz radiation induces non-thermal structural changes associated with Fröhlich condensation in a protein crystal. *Structural Dynamics* **2**, 054702 (2015).

19. B. G. Bobay, R. J. Thompson, J. A. Hoch, J. Cavanagh, Long range dynamic effects of point-mutations trap a response regulator in an active conformation. *FEBS Lett* **584**, 4203-4207 (2010).
20. M. W. Clarkson, A. L. Lee, Long-range dynamic effects of point mutations propagate through side chains in the serine protease inhibitor eglin c. *Biochemistry* **43**, 12448-12458 (2004).
21. M. W. Clarkson, S. A. Gilmore, M. H. Edgell, A. L. Lee, Dynamic coupling and allosteric behavior in a nonallosteric protein. *Biochemistry* **45**, 7693-7699 (2006).
22. D. M. Mittleman, Perspective: Terahertz science and technology. *J Appl Phys* **122**, (2017).
23. Y. Xu, M. Havenith, Perspective: Watching low-frequency vibrations of water in biomolecular recognition by THz spectroscopy. *J Chem Phys* **143**, (2015).
24. G. Acbas, K. A. Niessen, E. H. Snell, A. G. Markelz, Optical measurements of long-range protein vibrations. *Nature communications* **5**, 3076 (2014).
25. K. A. Niessen, M. Xu, A. G. Markelz, Terahertz optical measurements of correlated motions with possible allosteric function. *Biophys Rev* **7**, 201-216 (2015).
26. K. A. Niessen *et al.*, Moving in the Right Direction: Protein Vibrational Steering Function. *Biophys. J.* **112**, 933-942 (2017).
27. D. A. Turton *et al.*, Terahertz underdamped vibrational motion governs protein-ligand binding in solution. *Nature communications* **5**, 3999 (2014).
28. K. H. DuBay, G. R. Bowman, P. L. Geissler, Fluctuations within Folded Proteins: Implications for Thermodynamic and Allosteric Regulation. *Accounts Chem Res* **48**, 1098-1105 (2015).
29. D. Verma, D. J. Jacobs, D. R. Livesay, Changes in Lysozyme Flexibility upon Mutation Are Frequent, Large and Long-Ranged. *Plos Comput Biol* **8**, (2012).
30. M. J. Whitley, A. L. Lee, Frameworks for Understanding Long-Range Intra-Protein Communication. *Curr Protein Pept Sc* **10**, 116-127 (2009).
31. D. M. Leitner, Energy flow in proteins. *Annual review of physical chemistry* **59**, 233-259 (2008).
32. Z. Zhang, G. S. Agarwal, M. O. Scully, Quantum fluctuations in Fröhlich condensate of molecular vibrations driven far from equilibrium. *ArXiv e-prints*. 2018.
33. E. A. Merritt, Some B-eq are more equivalent than others. *Acta Crystallogr. A* **67**, 512-516 (2011).
34. E. A. Merritt, Expanding the model: anisotropic displacement parameters in protein structure refinement. *Acta Crystallogr. D* **55**, 1109-1117 (1999).
35. J. Foadi *et al.*, Clustering procedures for the optimal selection of data sets from multiple crystals in macromolecular crystallography. *Acta Crystallogr. D* **69**, 1617-1632 (2013).
36. A. R. Ortiz, C. E. M. Strauss, O. Olmea, MAMMOTH (Matching molecular models obtained from theory): An automated method for model comparison. *Protein Science* **11**, 2606-2621 (2002).
37. J. Walter *et al.*, On the disordered activation domain in trypsinogen. chemical labelling and low-temperature crystallography. *Acta Crystallogr. B* **38**, 1462 (1982).
38. D. M. Blow, J. J. Birktoft, B. S. Hartley, Role of a buried acid group in the mechanism of action of chymotrypsin. *Nature* **221**, 337-340 (1969).
39. R. Huber, W. Bode, Structural basis of the activation and action of trypsin. *Acc. Chem. Res.* **11**, 114-122 (1978).

40. W. Y. Wahlgren *et al.*, The catalytic aspartate is protonated in the Michaelis complex formed between trypsin and an in vitro evolved substrate-like inhibitor: a refined mechanism of serine protease action. *J. Biol. Chem.* **286**, 3587-3596 (2011).
41. K. Fodor *et al.*, Enzyme:substrate hydrogen bond shortening during the acylation phase of serine protease catalysis. *Biochemistry* **45**, 2114-2121 (2006).
42. D. Blow, So do we understand how enzymes work? *Struct Fold Des* **8**, R77-R81 (2000).
43. A. K. Dunker *et al.*, Intrinsically disordered protein. *J Mol Graph Model* **19**, 26-59 (2001).
44. A. K. Dunker *et al.*, The unfoldomics decade: an update on intrinsically disordered proteins. *Bmc Genomics* **9**, (2008).
45. P. Y. Chou, G. D. Fasman, Prediction of Protein Conformation. *Biochemistry* **13**, 222-245 (1974).
46. L. Graf, T. Molnar, J. Kardos, Z. Gaspari, G. Katona, The Role of Structural Flexibility and Stability in the Interaction of Serine Proteases with their Inhibitors. *Curr Protein Pept Sci* **16**, 521-531 (2015).
47. M. Akke, Conformational dynamics and thermodynamics of protein-ligand binding studied by NMR relaxation. *Biochem Soc T* **40**, 419-423 (2012).
48. M. Grognot, G. Gallot, Relative Contributions of Core Protein and Solvation Shell in the Terahertz Dielectric Properties of Protein Solutions. *J. Phys. Chem. B* **121**, 9508-9512 (2017).
49. A. Casanas *et al.*, EIGER detector: application in macromolecular crystallography. *Acta Cryst D* **72**, 1036-1048 (2016).
50. W. Kabsch, Xds. *Acta Crystallogr. D* **66**, 125-132 (2010).
51. M. D. Winn *et al.*, Overview of the CCP4 suite and current developments. *Acta Crystallogr. D* **67**, 235-242 (2011).
52. D. Liebschner, M. Dauter, A. Brzuszkiewicz, Z. Dauter, On the reproducibility of protein crystal structures: five atomic resolution structures of trypsin. *Acta Crystallogr. D* **69**, 1447-1462 (2013).
53. W. McKinney, paper presented at the Proceedings of the 9th Python in Science Conference 2010.
54. R. W. Grosse-Kunstleve, N. K. Sauter, N. W. Moriarty, P. D. Adams, The Computational Crystallography Toolbox: crystallographic algorithms in a reusable software framework. *J. Appl. Crystallogr.* **35**, 126-136 (2002).
55. H. Nguyen, D. A. Case, A. S. Rose, NGLview-interactive molecular graphics for Jupyter notebooks. *Bioinformatics* **34**, 1241-1242 (2018).
56. J. H. Ward, Hierarchical Grouping to Optimize an Objective Function. *J Am Stat Assoc* **58**, 236-& (1963).
57. C. S. Bury, J. C. Brooks-Bartlett, S. P. Walsh, E. F. Garman, Estimate your dose: RADDOSE-3D. *Protein Science* **27**, 217-228 (2018).
58. H. J. C. Berendsen, D. Vanderspoel, R. Vandrunen, Gromacs - a Message-Passing Parallel Molecular-Dynamics Implementation. *Comput Phys Commun* **91**, 43-56 (1995).
59. D. Van Der Spoel *et al.*, GROMACS: fast, flexible, and free. *J Comput Chem* **26**, 1701-1718 (2005).
60. M. J. Abraham *et al.*, GROMACS: High performance molecular simulations through multi-level parallelism from laptops to supercomputers. *SoftwareX* **1-2**, 19-25 (2015).

61. R. B. Best *et al.*, Optimization of the Additive CHARMM All-Atom Protein Force Field Targeting Improved Sampling of the Backbone phi, psi and Side-Chain chi(1) and chi(2) Dihedral Angles. *J Chem Theory Comput* **8**, 3257-3273 (2012).
62. A. D. MacKerell *et al.*, All-atom empirical potential for molecular modeling and dynamics studies of proteins. *J. Phys. Chem. B* **102**, 3586-3616 (1998).
63. A. D. MacKerell, Jr., M. Feig, C. L. Brooks, 3rd, Improved treatment of the protein backbone in empirical force fields. *J. Am. Chem. Soc.* **126**, 698-699 (2004).
64. G. A. Kaminski, R. A. Friesner, J. Tirado-Rives, W. L. Jorgensen, Evaluation and reparametrization of the OPLS-AA force field for proteins via comparison with accurate quantum chemical calculations on peptides. *Journal of Physical Chemistry B* **105**, 6474-6487 (2001).
65. W. L. Jorgensen, J. Chandrasekhar, J. D. Madura, R. W. Impey, M. L. Klein, Comparison of Simple Potential Functions for Simulating Liquid Water. *J Chem Phys* **79**, 926-935 (1983).
66. G. Bussi, D. Donadio, M. Parrinello, Canonical sampling through velocity rescaling. *J Chem Phys* **126**, (2007).
67. H. J. C. Berendsen, J. P. M. Postma, W. F. Vangunsteren, A. Dinola, J. R. Haak, Molecular-Dynamics with Coupling to an External Bath. *J Chem Phys* **81**, 3684-3690 (1984).
68. M. Parrinello, A. Rahman, Polymorphic Transitions in Single-Crystals - a New Molecular-Dynamics Method. *J Appl Phys* **52**, 7182-7190 (1981).
69. T. Darden, D. York, L. Pedersen, Particle Mesh Ewald - an N.Log(N) Method for Ewald Sums in Large Systems. *J Chem Phys* **98**, 10089-10092 (1993).

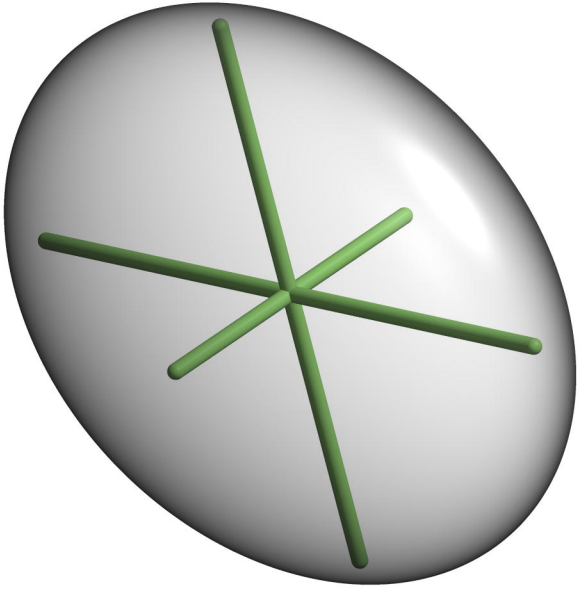

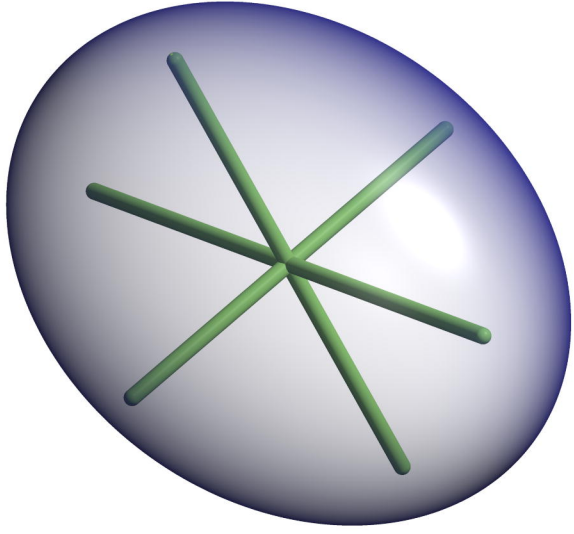

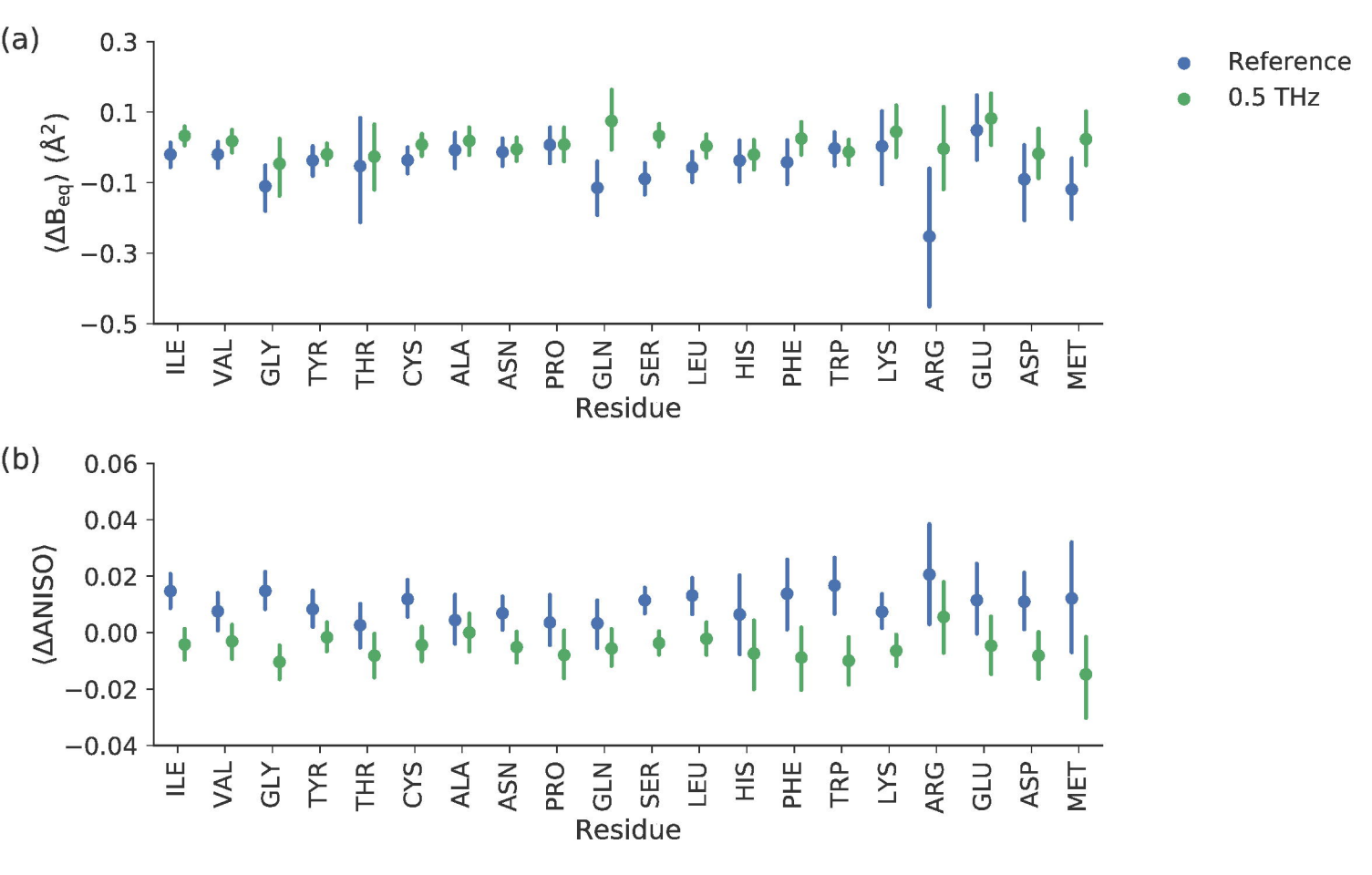
(a)
0.3
0.1
−0.1
−0.3
−0.5
⟨ΔB_eq⟩ (Å²)
ILE
VAL
GLY
TYR
THR
CYS
ALA
ASN
PRO
GLN
SER
LEU
HIS
PHE
TRP
LYS
ARG
GLU
ASP
MET
Residue
Reference
0.5 THz
(b)
0.06
0.04
0.02
0.00
−0.02
−0.04
⟨ΔANISO⟩
ILE
VAL
GLY
TYR
THR
CYS
ALA
ASN
PRO
GLN
SER
LEU
HIS
PHE
TRP
LYS
ARG
GLU
ASP
MET
Residue

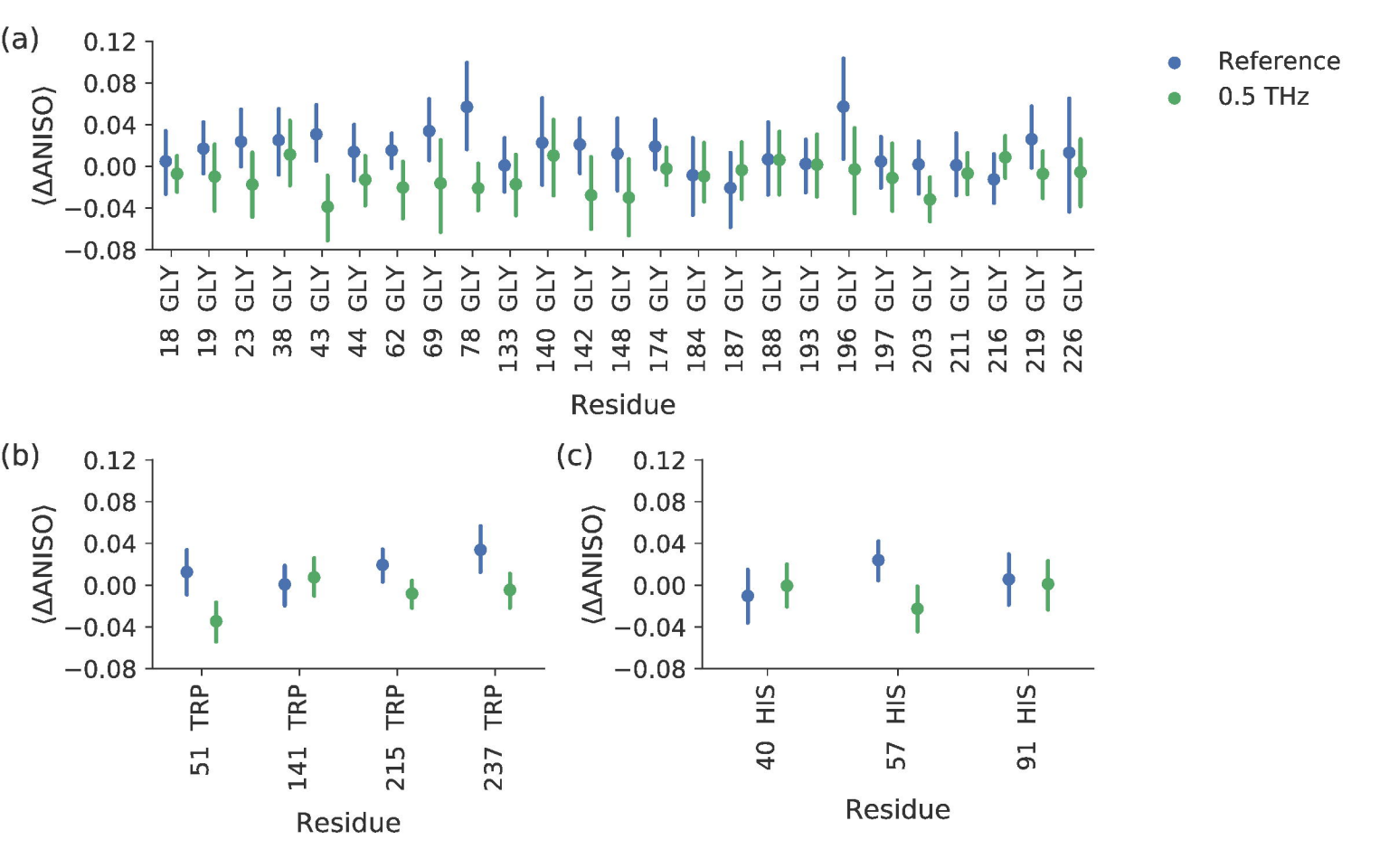
(a)
(b)
(c)
⟨ΔANISO⟩
0.12
0.08
0.04
0.00
−0.04
−0.08
Reference
0.5 THz
18 GLY
19 GLY
23 GLY
38 GLY
43 GLY
44 GLY
62 GLY
69 GLY
78 GLY
133 GLY
140 GLY
142 GLY
148 GLY
174 GLY
184 GLY
187 GLY
188 GLY
193 GLY
196 GLY
197 GLY
203 GLY
211 GLY
216 GLY
219 GLY
226 GLY
Residue
51 TRP
141 TRP
215 TRP
237 TRP
Residue
40 HIS
57 HIS
91 HIS
Residue

(a)

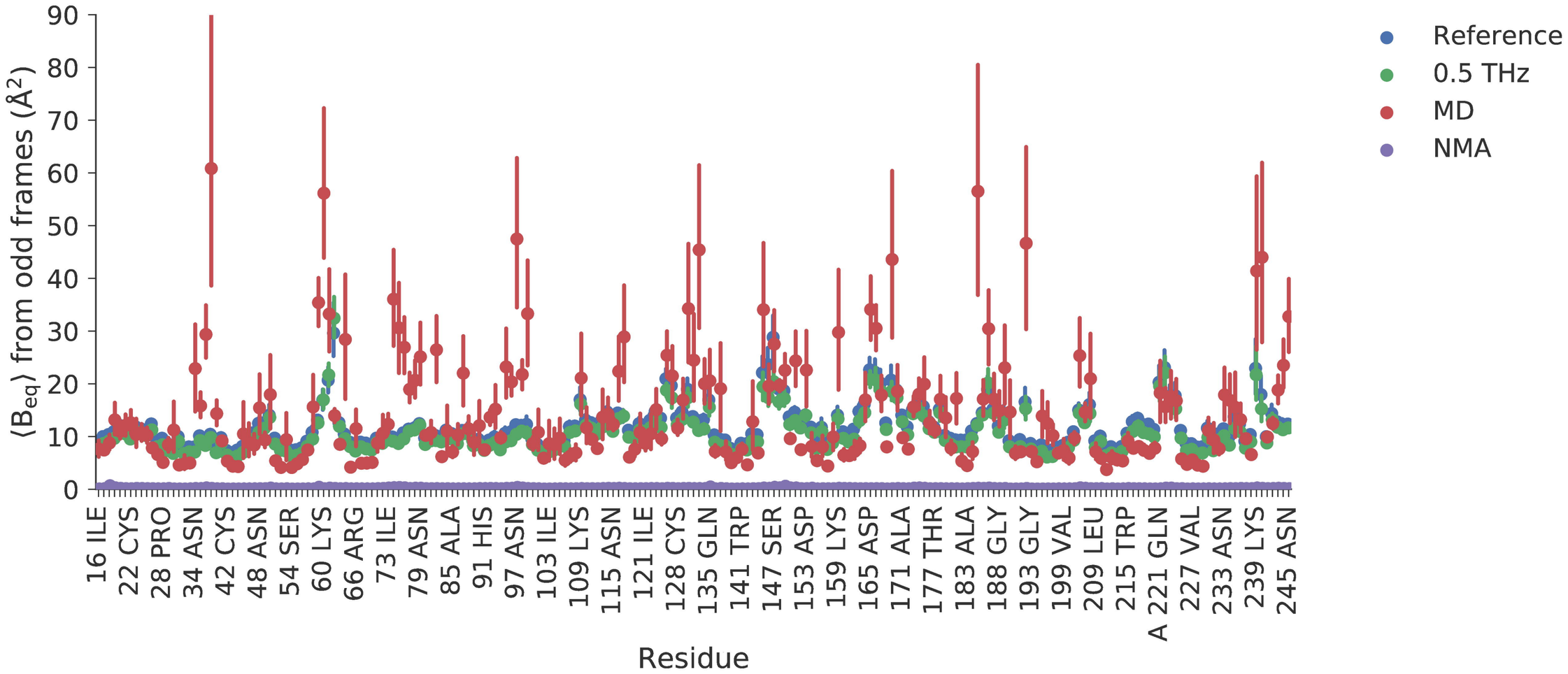

(b)

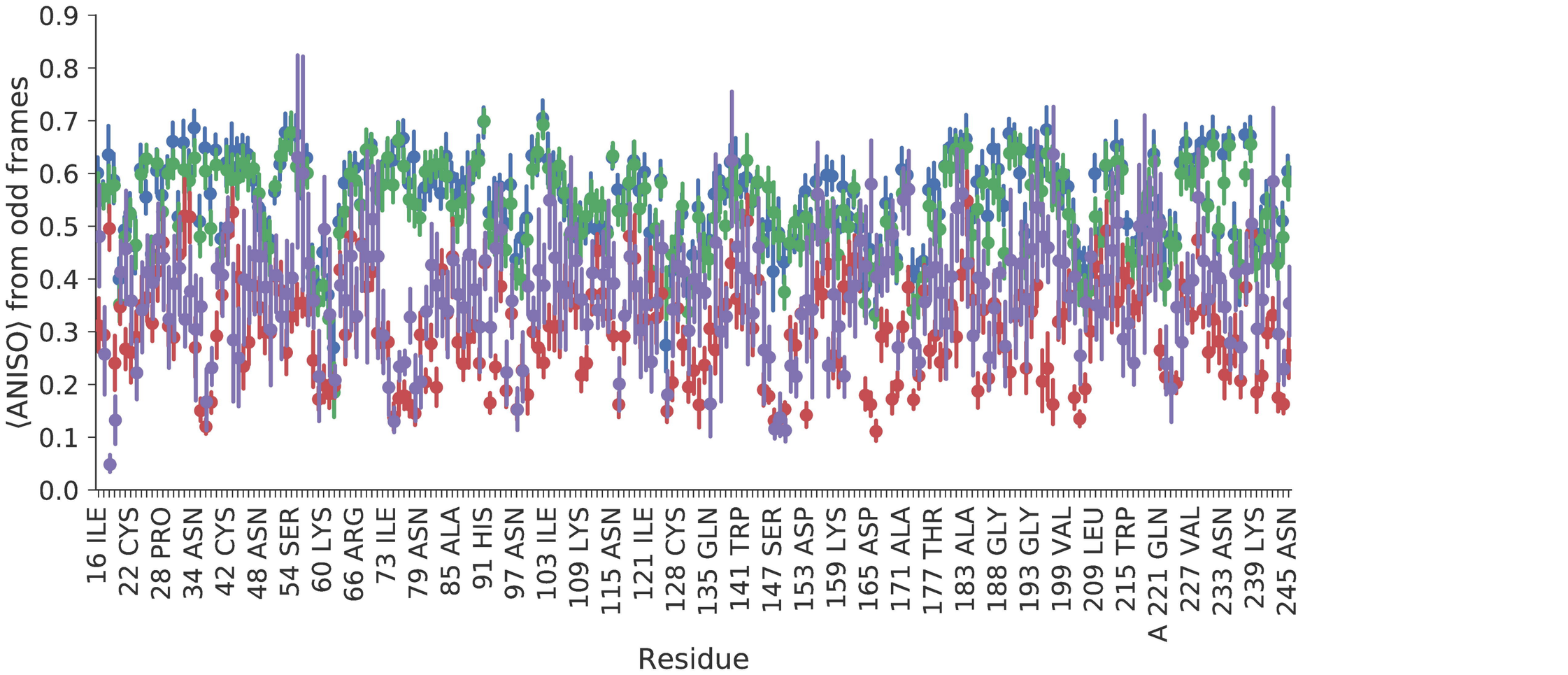

(c)

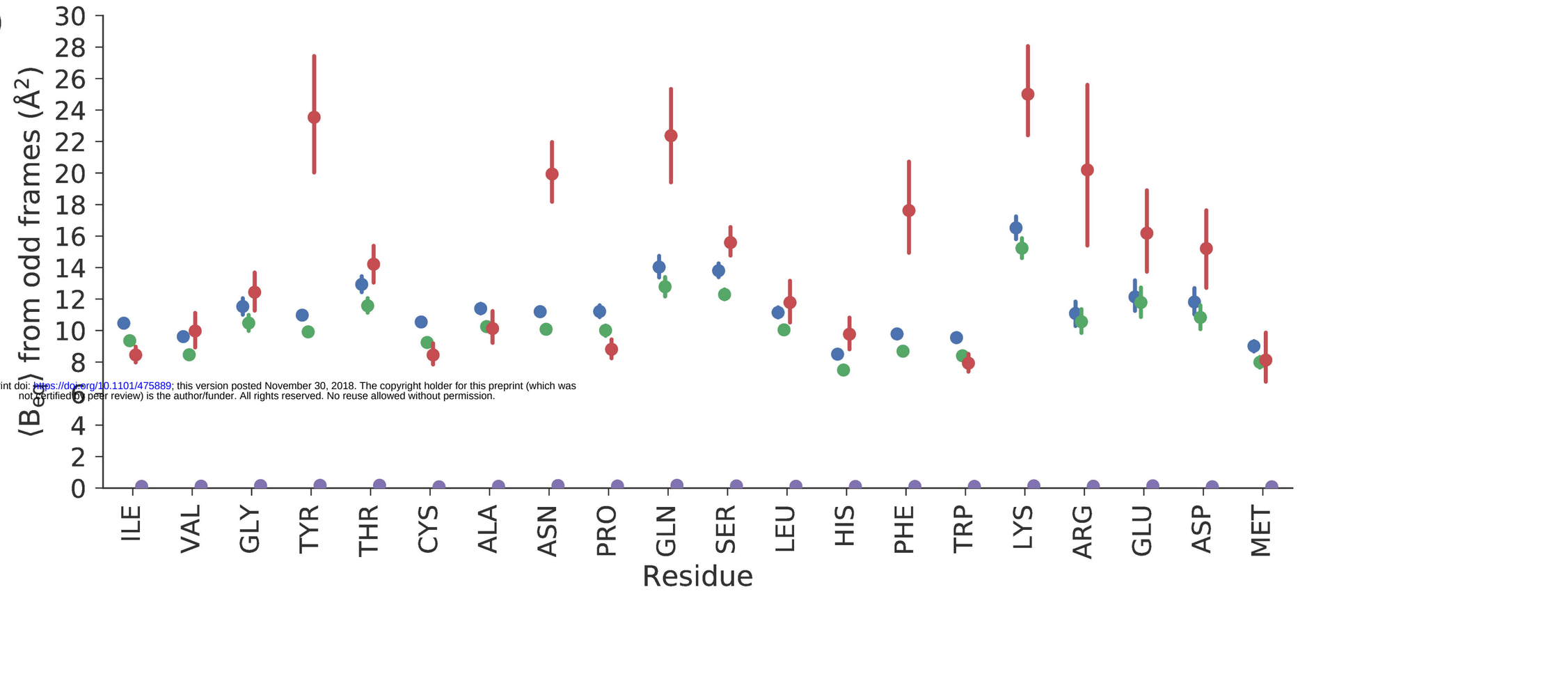

(d)

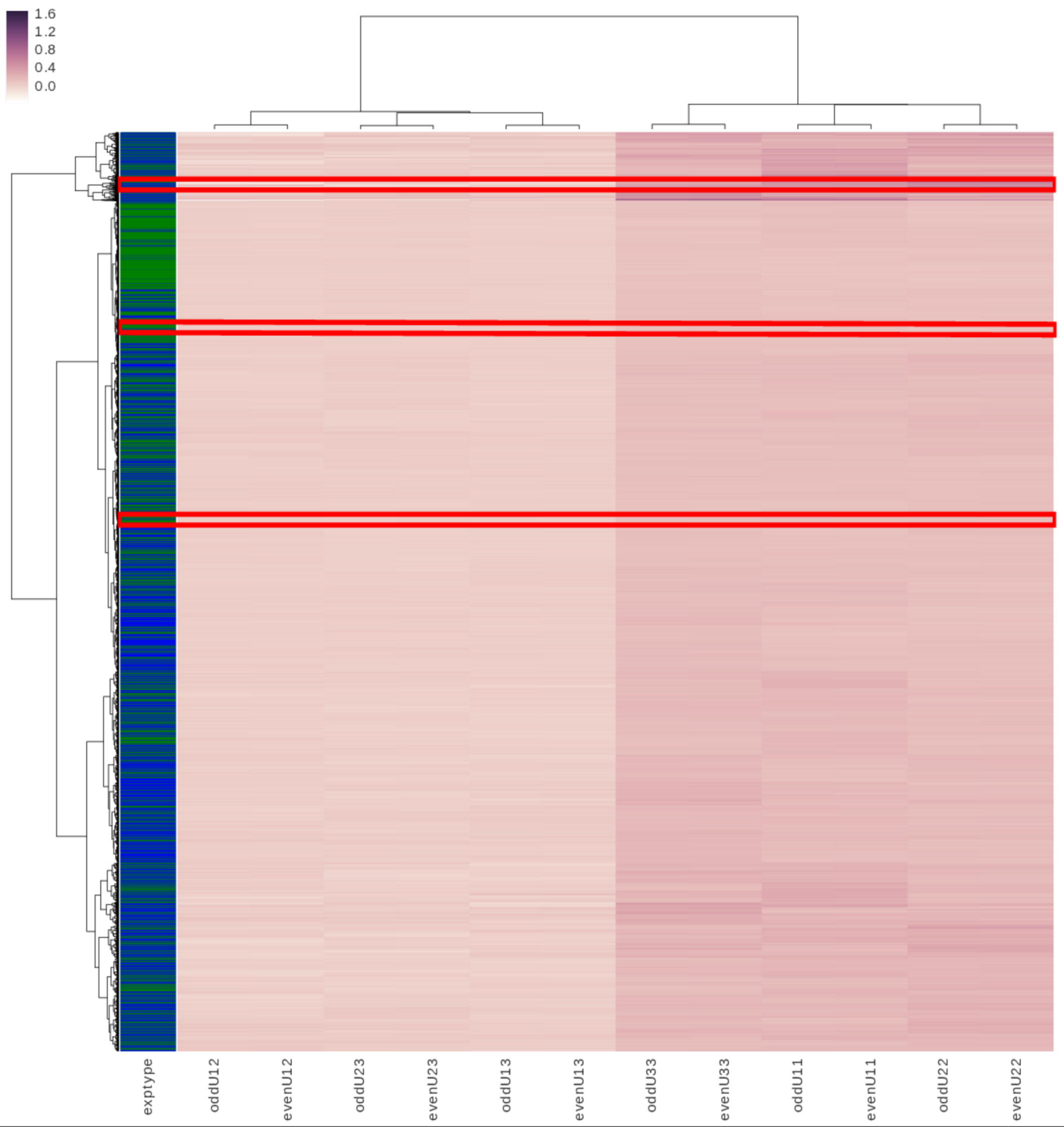
1.6
1.2
0.8
0.4
0.0
exptype
oddU12
evenU12
oddU23
evenU23
oddU13
evenU13
oddU33
evenU33
oddU11
evenU11
oddU22
evenU22

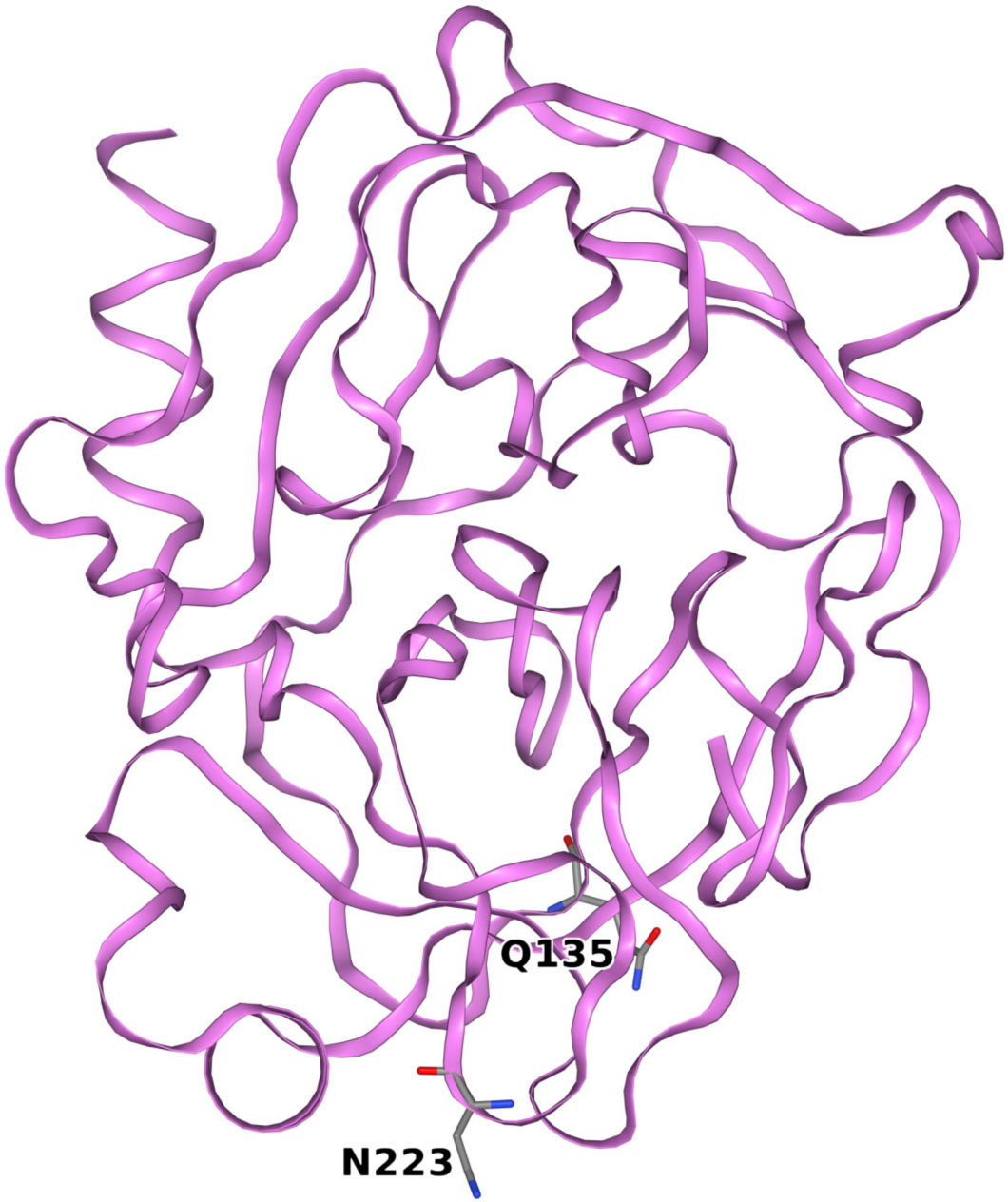
Q135
N223

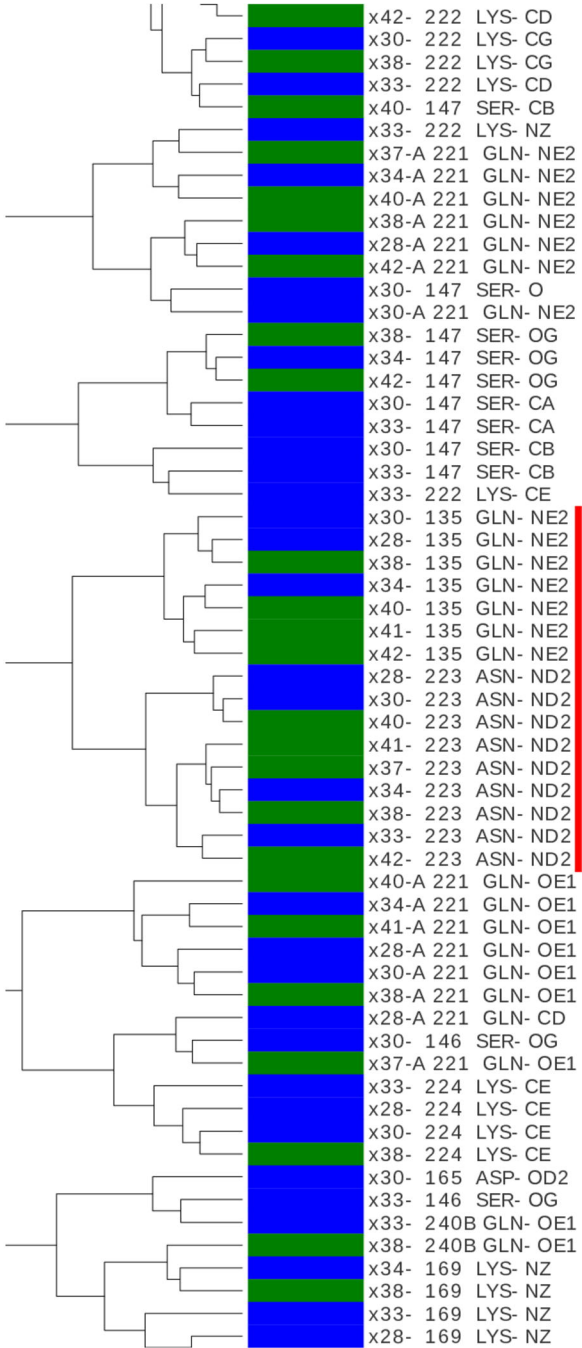
x42- 222 LYS- CD
x30- 222 LYS- CG
x38- 222 LYS- CG
x33- 222 LYS- CD
x40- 147 SER- CB
x33- 222 LYS- NZ
x37-A 221 GLN- NE2
x34-A 221 GLN- NE2
x40-A 221 GLN- NE2
x38-A 221 GLN- NE2
x28-A 221 GLN- NE2
x42-A 221 GLN- NE2
x30- 147 SER- O
x30-A 221 GLN- NE2
x38- 147 SER- OG
x34- 147 SER- OG
x42- 147 SER- OG
x30- 147 SER- CA
x33- 147 SER- CA
x30- 147 SER- CB
x33- 147 SER- CB
x33- 222 LYS- CE
x30- 135 GLN- NE2
x28- 135 GLN- NE2
x38- 135 GLN- NE2
x34- 135 GLN- NE2
x40- 135 GLN- NE2
x41- 135 GLN- NE2
x42- 135 GLN- NE2
x28- 223 ASN- ND2
x30- 223 ASN- ND2
x40- 223 ASN- ND2
x41- 223 ASN- ND2
x37- 223 ASN- ND2
x34- 223 ASN- ND2
x38- 223 ASN- ND2
x33- 223 ASN- ND2
x42- 223 ASN- ND2
x40-A 221 GLN- OE1
x34-A 221 GLN- OE1
x41-A 221 GLN- OE1
x28-A 221 GLN- OE1
x30-A 221 GLN- OE1
x38-A 221 GLN- OE1
x28-A 221 GLN- CD
x30- 146 SER- OG
x37-A 221 GLN- OE1
x33- 224 LYS- CE
x28- 224 LYS- CE
x30- 224 LYS- CE
x38- 224 LYS- CE
x30- 165 ASP- OD2
x33- 146 SER- OG
x33- 240B GLN- OE1
x38- 240B GLN- OE1
x34- 169 LYS- NZ
x38- 169 LYS- NZ
x33- 169 LYS- NZ
x28- 169 LYS- NZ

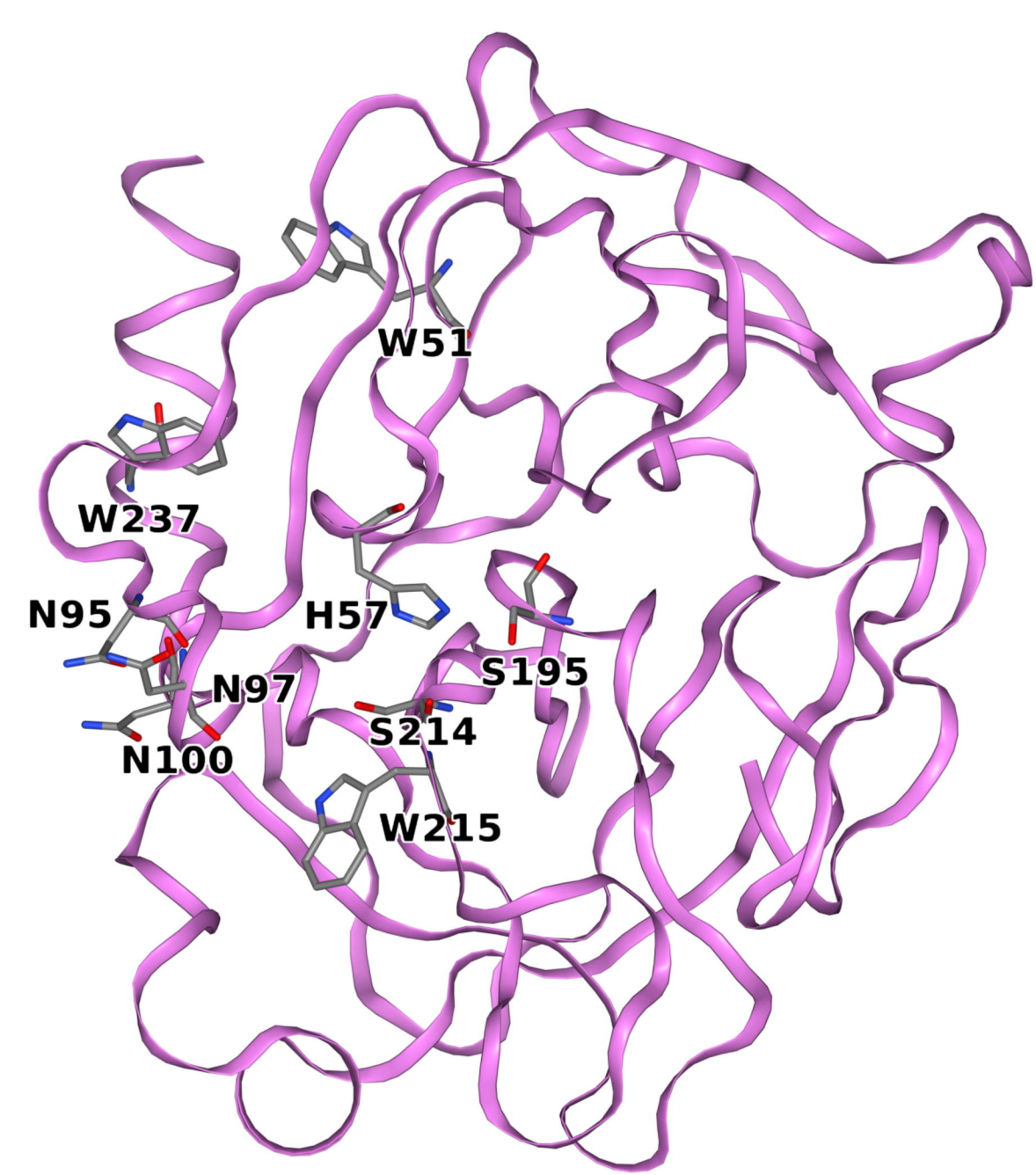
W51
W237
N95
H57
S195
N97
S214
N100
W215

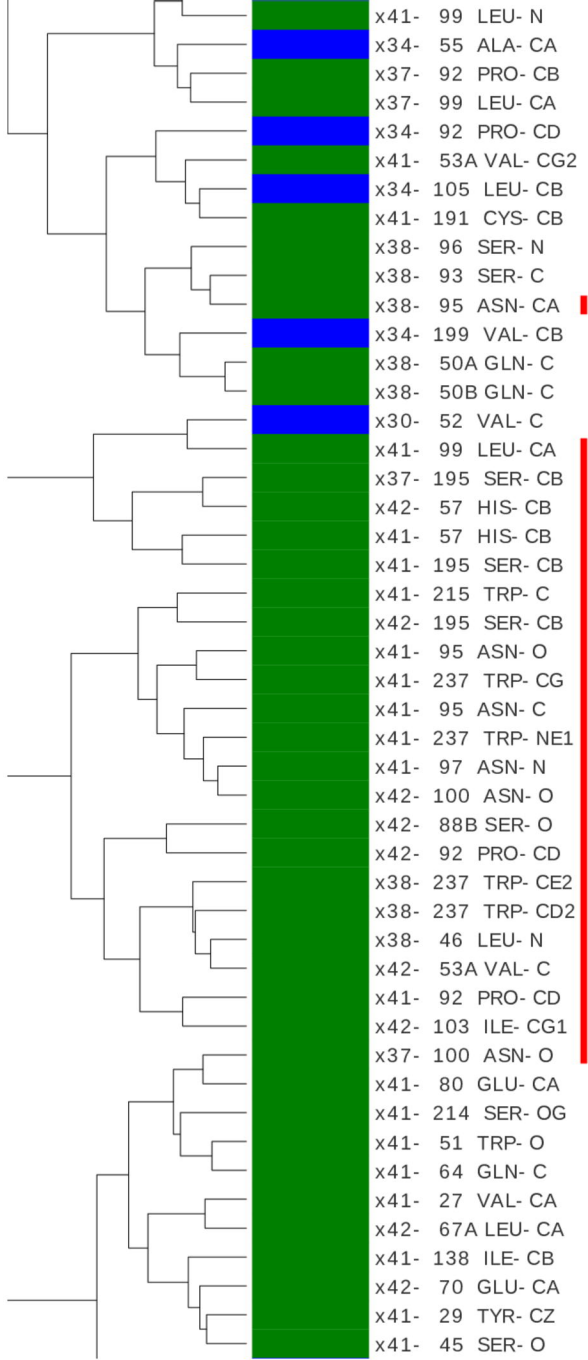
x41- 99 LEU- N
x34- 55 ALA- CA
x37- 92 PRO- CB
x37- 99 LEU- CA
x34- 92 PRO- CD
x41- 53A VAL- CG2
x34- 105 LEU- CB
x41- 191 CYS- CB
x38- 96 SER- N
x38- 93 SER- C
x38- 95 ASN- CA
x34- 199 VAL- CB
x38- 50A GLN- C
x38- 50B GLN- C
x30- 52 VAL- C
x41- 99 LEU- CA
x37- 195 SER- CB
x42- 57 HIS- CB
x41- 57 HIS- CB
x41- 195 SER- CB
x41- 215 TRP- C
x42- 195 SER- CB
x41- 95 ASN- O
x41- 237 TRP- CG
x41- 95 ASN- C
x41- 237 TRP- NE1
x41- 97 ASN- N
x42- 100 ASN- O
x42- 88B SER- O
x42- 92 PRO- CD
x38- 237 TRP- CE2
x38- 237 TRP- CD2
x38- 46 LEU- N
x42- 53A VAL- C
x41- 92 PRO- CD
x42- 103 ILE- CG1
x37- 100 ASN- O
x41- 80 GLU- CA
x41- 214 SER- OG
x41- 51 TRP- O
x41- 64 GLN- C
x41- 27 VAL- CA
x42- 67A LEU- CA
x41- 138 ILE- CB
x42- 70 GLU- CA
x41- 29 TYR- CZ
x41- 45 SER- O

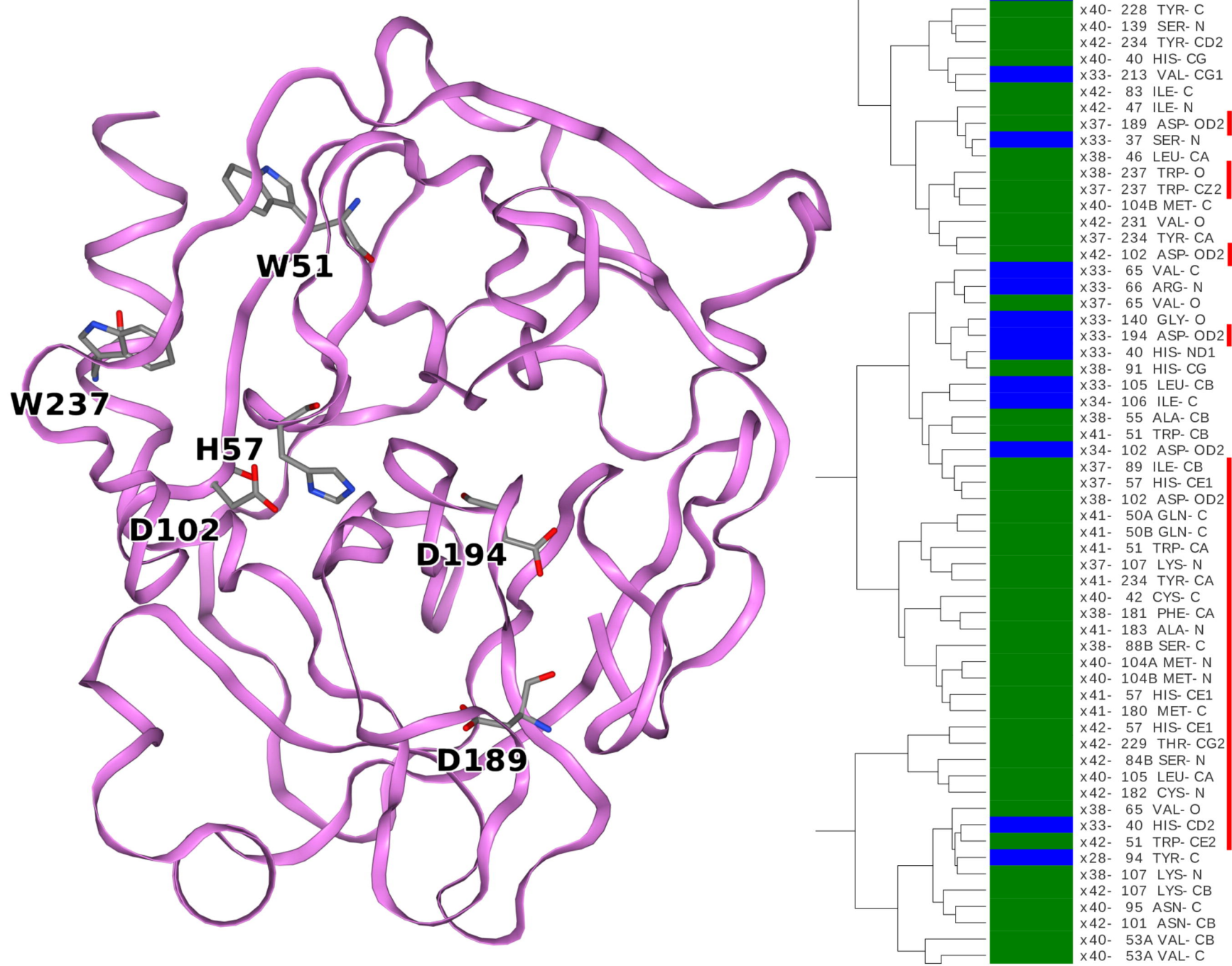
W51
W237
H57
D102
D194
D189
x40- 228 TYR- C
x40- 139 SER- N
x42- 234 TYR- CD2
x40- 40 HIS- CG
x33- 213 VAL- CG1
x42- 83 ILE- C
x42- 47 ILE- N
x37- 189 ASP- OD2
x33- 37 SER- N
x38- 46 LEU- CA
x38- 237 TRP- O
x37- 237 TRP- CZ2
x40- 104B MET- C
x42- 231 VAL- O
x37- 234 TYR- CA
x42- 102 ASP- OD2
x33- 65 VAL- C
x33- 66 ARG- N
x37- 65 VAL- O
x33- 140 GLY- O
x33- 194 ASP- OD2
x33- 40 HIS- ND1
x38- 91 HIS- CG
x33- 105 LEU- CB
x34- 106 ILE- C
x38- 55 ALA- CB
x41- 51 TRP- CB
x34- 102 ASP- OD2
x37- 89 ILE- CB
x37- 57 HIS- CE1
x38- 102 ASP- OD2
x41- 50A GLN- C
x41- 50B GLN- C
x41- 51 TRP- CA
x37- 107 LYS- N
x41- 234 TYR- CA
x40- 42 CYS- C
x38- 181 PHE- CA
x41- 183 ALA- N
x38- 88B SER- C
x40- 104A MET- N
x40- 104B MET- N
x41- 57 HIS- CE1
x41- 180 MET- C
x42- 57 HIS- CE1
x42- 229 THR- CG2
x42- 84B SER- N
x40- 105 LEU- CA
x42- 182 CYS- N
x38- 65 VAL- O
x33- 40 HIS- CD2
x42- 51 TRP- CE2
x28- 94 TYR- C
x38- 107 LYS- N
x42- 107 LYS- CB
x40- 95 ASN- C
x42- 101 ASN- CB
x40- 53A VAL- CB
x40- 53A VAL- C